

# Abstract

BUSNARDO, DAVID MARC. LIDAR-Aided Inertial Navigation over Rough Terrain.  
(Under the direction of Dr. Robert H. Tolson.)

In support of NASA's Autonomous Landing and Hazard Avoidance Technology project, an existing extended Kalman Filter (EKF) routine has been tested and retuned to estimate the position, velocity, and orientation of a spacecraft on trajectories over rough terrain. The original filter, which performed well over flat surfaces, has been modified to provide more accurate state estimates over such terrains. The filter combines measurements of range and Doppler velocity from an on-board Light Detection and Ranging (LIDAR) system with measurements of acceleration and angular velocity from an inertial measurement unit. The high-precision LIDAR measurements will allow both manned and unmanned spacecraft to land accurately and safely near sites that may be scientifically interesting but potentially hazardous. The filter was tested for robustness and accuracy using a simplified simulation of Apollo lunar landings during the final translation and touchdown.

LIDAR-Aided Inertial Navigation over Rough Terrain

by  
David Marc Busnardo

A thesis submitted to the Graduate Faculty of  
North Carolina State University  
in partial fulfillment of the  
requirements for the Degree of  
Master of Science

Aerospace Engineering

Raleigh, North Carolina

2011

APPROVED BY:

---

Fred DeJarnette

---

Andre Mazzoleni

---

Robert Tolson  
Chair of Advisory Committee

# Dedication

For my family

# Biography

David M. Busnardo was born in Augusta, Georgia in 1986. He attended schools in Columbia, South Carolina and received his Bachelor of Science in Aerospace Engineering from the University of Tennessee at Knoxville in 2008. In July 2008, he began study for a Master of Science in Aerospace Engineering from North Carolina State University, while working as a graduate research assistant for the Department of Mechanical and Aerospace Engineering. He has been employed in this position since, working in residence at the National Institute of Aerospace and NASA Langley Research Center.

# Acknowledgements

There are a number of people I'd like to thank, first of all my advisor Dr. Robert Tolson. His constant support, extensive knowledge and interpretation were critical to the completion of this work. I also wish to thank Dr. Fred DeJarnette and Dr. Andre Mazzoleni for their help and for agreeing to serve on my committee.

I must also particularly thank Dr. Farzin Amzajerian of NASA Langley Research Center, principal investigator of this project, for his sponsorship, constant support, and insight. I also owe a great deal to Diego Pierrottet of Coherent Applications, Inc. for providing test data and valuable assistance. I am also deeply indebted to Matthew Aitken, who developed the original filter and simulation discussed in this work.

Last of all I especially want to thank my family. Without you I would not have accomplished anything. I am the person that I am today because of your constant love and support. You've provided so much for me, including supporting my education and giving me the best possible example of how to live my life. Mom, Dad, Mike, this work is as much yours as it is mine.

# Table of Contents

<b>List of Tables</b> .....	vi
<b>List of Figures</b> .....	vii
<b>Nomenclature and Abbreviations</b> .....	viii
<b>1 Introduction</b> .....	1
<b>2 Flat Surface Studies</b> .....	5
<b>3 Bumpy Terrains</b> .....	13
<b>4 Washboard Terrains</b> .....	27
<b>5 Step Terrains</b> .....	38
<b>6 Conclusions and Future Work</b> .....	43
<b>References</b> .....	45

# List of Tables

<b>Table 1. Adjusted Filter Parameters.....</b>	<b>22</b>
---	-----------

# List of Figures

<b>Figure 1. LIDAR beam geometry .....</b>	<b>1</b>
<b>Figure 2. Spacecraft true state for flat surface simulations.....</b>	<b>6</b>
<b>Figure 3. LIDAR ground tracks for simulated trajectory. ....</b>	<b>7</b>
<b>Figure 4. Errors in estimated state for varying LIDAR polar angles.....</b>	<b>8</b>
<b>Figure 5. Errors in estimated states for beam and head assembly misalignments..</b>	<b>10</b>
<b>Figure 6. Errors in estimated states for limited data types.....</b>	<b>12</b>
<b>Figure 7. Simulated trajectory over bumpy terrain. ....</b>	<b>16</b>
<b>Figure 8. Position estimate and error versus time with original filter parameters. .</b>	<b>18</b>
<b>Figure 9. Velocity estimate and error versus time with original filter parameters..</b>	<b>19</b>
<b>Figure 10. Accelerometer bias estimate and error versus time with original filter parameters. ....</b>	<b>19</b>
<b>Figure 11. Gyro bias estimate and error versus time with original filter parameters. ....</b>	<b>20</b>
<b>Figure 12. Orientation estimate and error versus time with original filter parameters. ....</b>	<b>20</b>
<b>Figure 13. Position estimate and error versus time with new filter parameters.....</b>	<b>23</b>
<b>Figure 14. Velocity estimate and error versus time with new filter parameters.....</b>	<b>23</b>
<b>Figure 15. Accelerometer bias estimate and error versus time with new filter parameters. ....</b>	<b>24</b>
<b>Figure 16. Gyro bias estimate and error versus time with new filter parameters....</b>	<b>24</b>
<b>Figure 17. Orientation estimate and error versus time with new filter parameters.</b>	<b>25</b>
<b>Figure 18. Range measurement differences between true surface and assumed flat surface, actual (top) and Doppler-derived estimation (bottom). ....</b>	<b>26</b>
<b>Figure 19. Sample washboard terrain, 5m amplitude by 100m wavelength. ....</b>	<b>28</b>
<b>Figure 20. Effect of terrain height on altitude gain, 100m wavelength terrains, 300m altitude. ....</b>	<b>29</b>
<b>Figure 21. Effect of state noise on altitude gain, 1m by 100m terrain, 300m altitude. ....</b>	<b>31</b>
<b>Figure 22. Effect of spacecraft altitude on altitude gain, 5m x 100m terrain.....</b>	<b>33</b>
<b>Figure 23. Effect of LIDAR phase difference on altitude gain, 1m x 100m terrain, 10 m/s.....</b>	<b>34</b>
<b>Figure 24. Steady-state z-accelerometer bias error, 1m x 100m terrain, 10 m/s.....</b>	<b>35</b>
<b>Figure 25. Steady-state y-gyro bias error, 1m x 100m terrain, 10 m/s.....</b>	<b>36</b>
<b>Figure 26. Steady-state pitch error, 1m x 100m terrain, 10 m/s. ....</b>	<b>36</b>
<b>Figure 27. Influence of step terrain on position estimates. ....</b>	<b>39</b>
<b>Figure 28. Influence of step terrain on velocity estimates. ....</b>	<b>40</b>
<b>Figure 29. Influence of step terrain on accelerometer bias estimates. ....</b>	<b>40</b>
<b>Figure 30. Influence of step terrain on gyro bias estimates. ....</b>	<b>41</b>
<b>Figure 31. Influence of step terrain on orientation estimates. ....</b>	<b>41</b>

# Nomenclature and Abbreviations

## Symbols

All vectors are 3x1 and all matrices are 3x3 unless otherwise noted.

$A$	rotation from navigation frame to vehicle body frame
$a$	net body acceleration vector
$a_m$	measured net body acceleration vector
$b_a$	accelerometer drift-rate bias vector
$b_g$	gyroscope drift-rate bias vector
$F$	continuous-time state transition matrix (15x15)
$G$	input noise sensitivity matrix (15x12)
$g$	gravitational acceleration vector
$H$	measurement sensitivity matrix (6x15)
$h_t$	sinusoidal terrain height
$K$	Kalman gain matrix (15x6)
$N$	discrete-time state noise covariance matrix (15x15)
$p$	position vector
$P$	state error covariance matrix (16x16)
$P_k^-$	predicted covariance at time $t_k$ (16x16)
$P_k^+$	updated covariance after measurement at time $t_k$ (16x16)
$Q$	continuous-time state noise covariance matrix (12x12)
$q$	attitude quaternion
$R$	measurement noise covariance matrix (6x6)
$s$	range coordinate
$u$	measurement noise (6x1)
$v$	velocity vector
$w$	state noise (12x1)
$x$	state vector (16x1)
$\hat{x}$	state estimate (16x1)
$\hat{x}_k^-$	predicted state estimate at time $t_k$ (16x1)
$\hat{x}_k^+$	updated state estimate after measurement at time $t_k$ (16x1)
$z$	measurement vector (6x1)
$\Delta x$	state error vector (16x1)
$\Phi$	discrete-time state transition matrix (15x15)
$\omega$	body angular velocity vector
$\omega_e$	Earth angular velocity vector
$\omega_m$	measured body angular velocity vector
$\lambda_t$	sinusoidal terrain wavelength

## Subscripts

<i>a</i>	accelerometer
<i>e</i>	Earth
<i>g</i>	gyroscope
<i>k</i>	value at the <i>k</i> -th time step
<i>m</i>	measured value
0	initial value

## Superscripts

-	predicted value
+	updated value

## Abbreviations

NASA	National Aeronautics and Space Administration
ALHAT	Autonomous Landing and Hazard Avoidance Technology
LaRC	Langley Research Center
LIDAR	Light detection and ranging
EKF	extended Kalman filter
IMU	inertial measurement unit

# 1 Introduction

The results presented in this document were conducted in support of NASA's Autonomous Landing and Hazard Avoidance Technologies Technology (ALHAT) project. The objectives of ALHAT are to create descent and landing systems for manned or unmanned missions which can land within tens of meters of pre-deployed assets or surface features of interest, as well as the ability to land in sites which may contain hazards such as slopes, rocks, and craters (Amzajerian, Johnson). In support of this goal, NASA Langley Research Center (LaRC) has developed a three-beam light detection and ranging (LIDAR) system to be used in aided inertial navigation. Each beam is directed at a polar angle of  $22.5^\circ$  from the negative z-axis, and the beams are separated from one another by a clock angle of  $120^\circ$  (Pierrottet). Each beam measures distance to the ground (range) and line of sight velocity. Figure 1 shows the geometry of the LIDAR system.

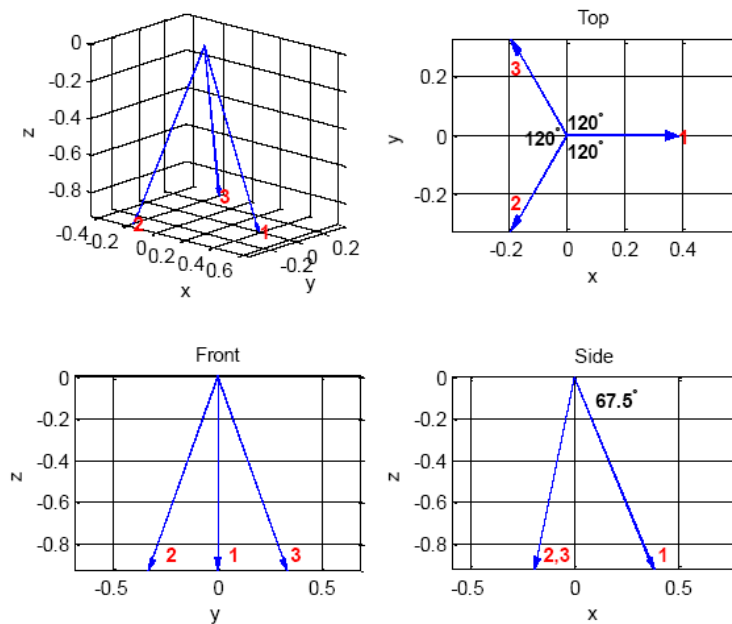


Figure 1. LIDAR beam geometry (Aitken).

An extended Kalman filter (EKF) was developed by Matthew Aitken to be used with this LIDAR system. This filter uses LIDAR range and Doppler measurements, as well as measurements from an inertial measurement unit (IMU) to update the state of a spacecraft. The estimated states include the inertial position and velocity, orientation, and biases that may be present in the accelerometers and gyros.

The development below follows Aitken, drawing from Lefferts, Trawny, and Vallado. In general, the extended Kalman filter is described with the following equations. The system is governed by the state equation

$$\frac{d}{dt} \mathbf{x}(t) = \mathbf{f}(\mathbf{x}(t), t) + \mathbf{g}(\mathbf{x}(t), t) \mathbf{w}(t)$$

in which  $\mathbf{x}(t)$  is the state vector and  $\mathbf{w}(t)$  is a Gaussian white noise vector. The state error vector satisfies the equation

$$\frac{d}{dt} \Delta \mathbf{x}(t) = \mathbf{F}(t) \Delta \mathbf{x}(t) + \mathbf{G}(t) \mathbf{w}(t)$$

which can be integrated to find

$$\Delta \mathbf{x}(t) = \Phi(t, t_0) \Delta \mathbf{x}(t_0) + \int_0^t \Phi(t, t') \mathbf{G}(t') \mathbf{w}(t') dt'$$

The predicted covariance matrix satisfies the matrix Riccati equation

$$\frac{d}{dt} P(t) = \mathbf{F}(t) P(t) + P(t) \mathbf{F}^T(t) + \mathbf{G}(t) \mathbf{Q}(t) \mathbf{G}^T(t)$$

which can be integrated to find

$$P(t) = \Phi(t, t_0) P(t_0) \Phi^T(t, t_0) + N(t, t_0)$$

The state estimate and covariance from time  $t_k$  are mapped into the next measurement time,  $t_{k+1}$  using

$$\hat{\mathbf{x}}_{k+1}^- = \varphi(t_{k+1}, \hat{\mathbf{x}}_k^+, t_k)$$

$$P_{k+1}^- = \Phi_k P_k^+ \Phi_k^T + N_k$$

The measurement vector  $z_k$  at time  $t_k$  is related to the state by

$$z_k = h(x_k) + u_k$$

With the Kalman gain matrix defined by

$$K_k = P_k^- H_k^T (H_k P_k^- H_k^T + R_k)^{-1}$$

The estimate and covariance are updated at time  $t_k$  using the measurement  $z_k$  according to

$$\hat{x}_k = \hat{x}_k^- + K_k [z_k - h(\hat{x}_k^-)]$$

$$P_k^+ = (I - K_k H_k) P_k^- (I - K_k H_k)^T + K_k R_k K_k^T$$

This process is repeated for each iteration using the new measurement at the next time step.

In this filter, the state vector includes the position, velocity, attitude quaternion, and bias vectors

$$x(t) = \begin{bmatrix} p \\ v \\ b_a \\ q \\ b_g \end{bmatrix}$$

The predicted version of the state equation is defined by

$$\frac{d}{dt} \hat{x}(t) = \frac{d}{dt} \begin{bmatrix} \hat{p} \\ \hat{v} \\ \hat{b}_a \\ \hat{q} \\ \hat{b}_g \end{bmatrix} = \begin{bmatrix} \hat{v} \\ \hat{A}^T \hat{a} + g - 2[\omega_e \times] \hat{v} - [\omega_e \times]^2 \hat{p} \\ 0 \\ \frac{1}{2} \Omega(\hat{\omega}) \hat{q} \\ 0 \end{bmatrix}$$

where  $\hat{a} = a_m - \hat{b}_a$ ,  $\hat{\omega} = \omega_m - \hat{b}_g - \hat{A} \omega_e$ , and  $\hat{A}$  is the direction cosine matrix which corresponds to the predicted attitude quaternion.

The continuous-time state transition matrix  $F$  and the input noise sensitivity matrix  $G$  are given by

$$F = \begin{bmatrix} 0_{3 \times 3} & I_{3 \times 3} & 0_{3 \times 3} & 0_{3 \times 3} & 0_{3 \times 3} \\ 0_{3 \times 3} & 0_{3 \times 3} & -\hat{A}^T & -\hat{A}^T [\hat{a} \times] & 0_{3 \times 3} \\ 0_{3 \times 3} & 0_{3 \times 3} & 0_{3 \times 3} & 0_{3 \times 3} & 0_{3 \times 3} \\ 0_{3 \times 3} & 0_{3 \times 3} & 0_{3 \times 3} & -[\omega \times] & -I_{3 \times 3} \\ 0_{3 \times 3} & 0_{3 \times 3} & 0_{3 \times 3} & 0_{3 \times 3} & 0_{3 \times 3} \end{bmatrix}, G = \begin{bmatrix} 0_{3 \times 3} & 0_{3 \times 3} & 0_{3 \times 3} & 0_{3 \times 3} \\ -\hat{A}^T & 0_{3 \times 3} & 0_{3 \times 3} & 0_{3 \times 3} \\ 0_{3 \times 3} & I_{3 \times 3} & 0_{3 \times 3} & 0_{3 \times 3} \\ 0_{3 \times 3} & 0_{3 \times 3} & -I_{3 \times 3} & 0_{3 \times 3} \\ 0_{3 \times 3} & 0_{3 \times 3} & 0_{3 \times 3} & I_{3 \times 3} \end{bmatrix}$$

The discrete-time state transition matrix at  $t_k$  is given by

$$\Phi_k = \exp\left(\int_{t_k}^{t_{k+1}} F(t') dt'\right)$$

and the discrete-time noise covariance matrix  $N_k$  is given by

$$N_k = \int_{t_k}^{t_{k+1}} \Phi(t_{k+1}, t') G(t') Q G^T(t') \Phi^T(t_{k+1}, t') dt'$$

The estimate of the state vector and covariance is updated at each time step  $t_k$  with the measurement  $z_k$  using the equations detailed previously.

Numerous studies were conducted using this filter and its original tuning to test the response of the filter over rough terrains. With the original tuning, the state of the spacecraft was well estimated over a flat surface, but suffered when terrain features were introduced. The studies performed included several studies of the filter performance over flat terrain, including variations in the LIDAR geometry, beam misalignments, and loss of either range or Doppler measurements. The filter was also tested over simulated terrains with hemispherical bumps, sinusoidal hills, and mesa-like steps. The result of these studies was a retuned filter which is able to more accurately estimate the state of the spacecraft over various rough terrains.

## 2 Flat Surface Studies

Several studies were conducted using the original filter to explore how changes in the LIDAR beam geometry or limited data would influence the estimate of the state for trajectories over a flat surface. These studies included varying the polar angle of the LIDAR beams from the current  $22.5^\circ$ , including small misalignments in the beam directions, and limiting the gathered LIDAR data to only range or Doppler measurements. In this simulation, based on the final touchdown phase in lunar landing as described in Bennett et al., the surface is assumed to be flat, at an altitude of 0m. The navigation z-axis is normal to the surface and directed upward. The x-axis is an arbitrary direction in the surface of the plane, and the y-axis completes the right-hand coordinate system. The navigation coordinate system is taken to be inertial; the rotation of the planet was ignored. The IMU axes are assumed identical to that of the vehicle body system.

Planetary gravitational acceleration is a constant  $g = 1.625 \text{ m/s}^2$ , and acts opposite the navigation z-axis. The simulation initial conditions were taken as follows: altitude = 337 m, velocity = 20.2 m/s, flight path angle  $0^\circ$ , yaw =  $45^\circ$ , pitch =  $-14^\circ$ , and roll =  $0^\circ$ . The vehicle experiences a constant thrust of 0.98g along the body z-axis, and a constant pitch rate of 0.002443 rad/s. These conditions were selected so that the spacecraft would land upright on the surface with no x- or y-velocity, and minimal z-velocity. In this simulation, the initial estimate of the state was chosen to vary from the true state. The initial position error is +100 m in all directions, while the initial velocity error was selected to be +5 m/s in all directions. The yaw, pitch, and roll vary from the true state by -3, +5, and +5 degrees respectively. The accelerometer and gyro biases were initially estimated at zero. Figure 2 shows the true state of the spacecraft throughout the

trajectory, and Figure 3 shows an overhead view. The LIDAR ground tracks are also shown. The circles along the ground tracks are placed every ten seconds, as a visual representation of the velocity.

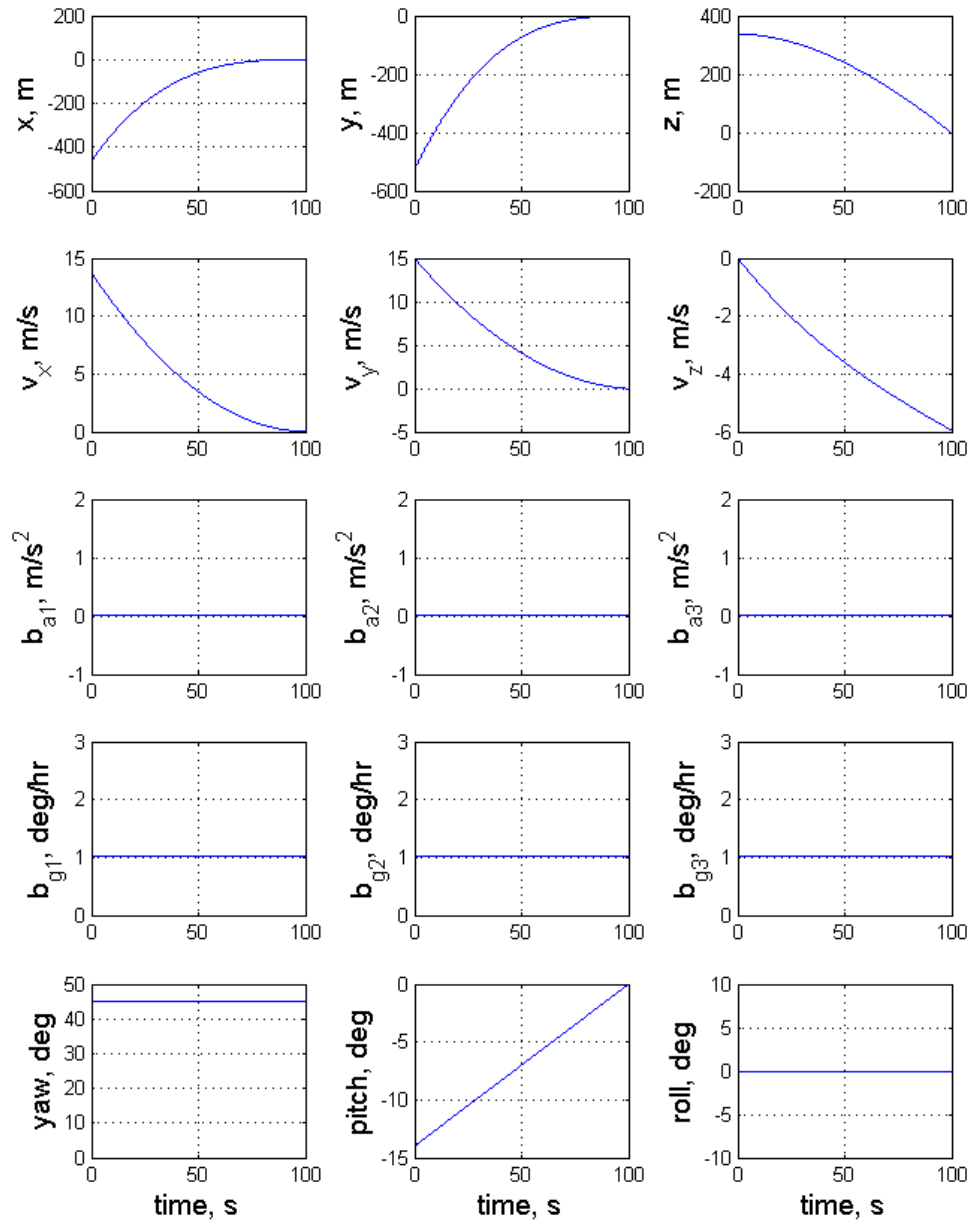


Figure 2. Spacecraft true state for flat surface simulations.

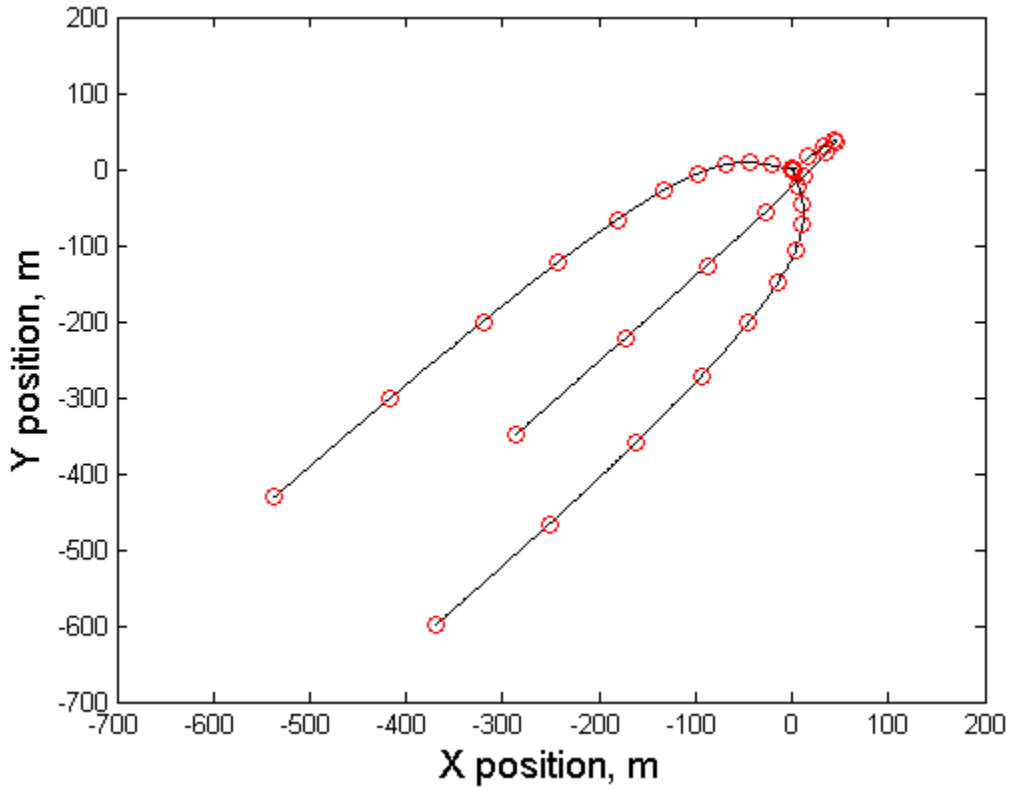


Figure 3. LIDAR ground tracks for simulated trajectory.

First, the polar angle of the LIDAR beams was varied between  $10^\circ$  and  $50^\circ$  to determine if the current  $22.5^\circ$  was near optimal in estimating the spacecraft state, or if it should be changed. For each polar angle, LIDAR measurements were generated using the above simulation and the state of the spacecraft was estimated. Figure 4, below, shows the errors in the estimated state for polar angles of  $10^\circ$ ,  $30^\circ$ , and  $50^\circ$ .

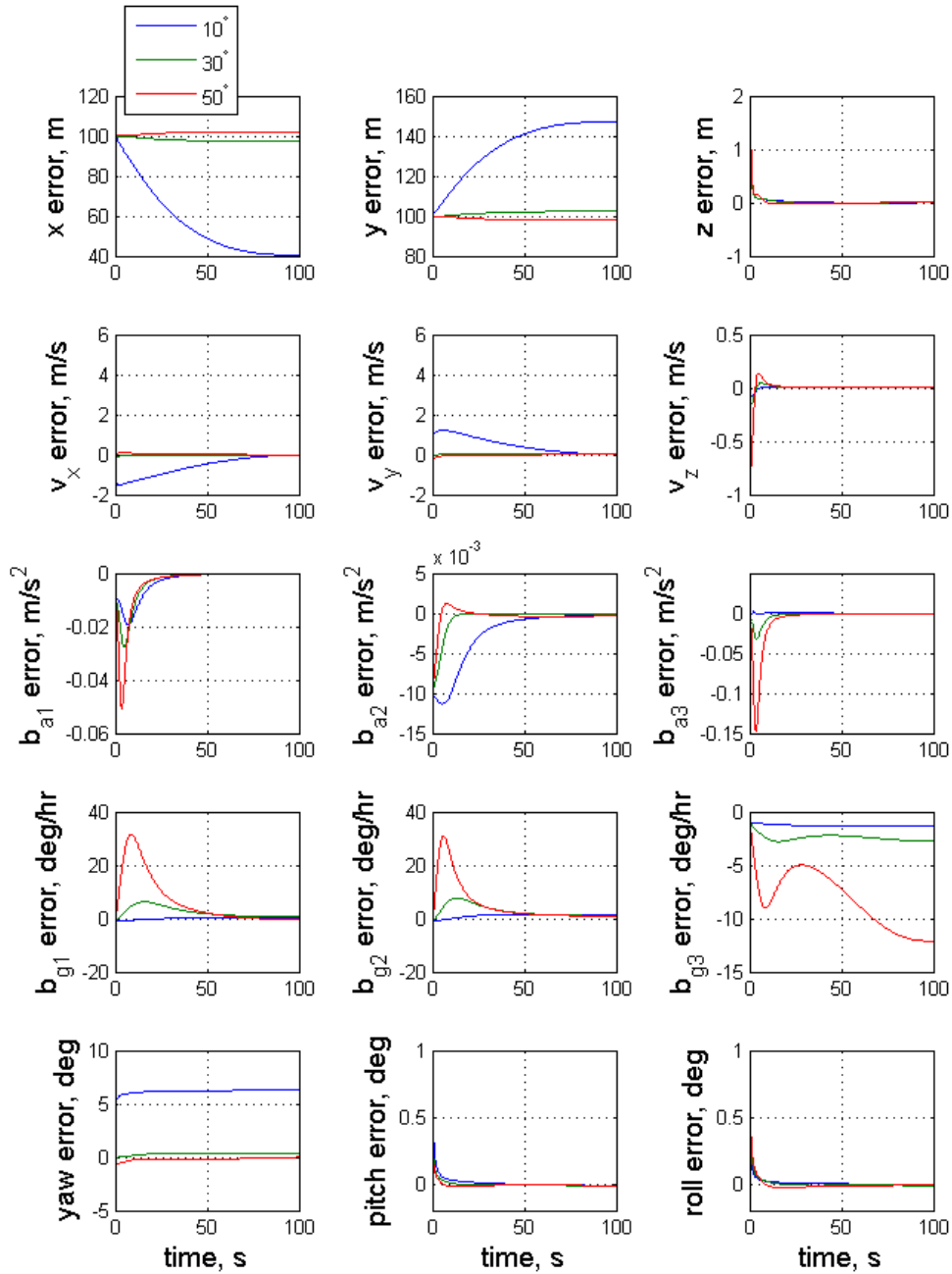


Figure 4. Errors in estimated state for varying LIDAR polar angles.

For small polar angles such as 10-15°, the filter estimates altitude and vertical velocity well, at the expense of the  $x$  and  $y$  directions. Accelerometer and gyro biases are also generally better estimated. With larger polar angles of 40-50°, the filter is slightly

slower in refining estimates of altitude and vertical velocity, but estimates in other directions are significantly improved. However, the accelerometer and gyro biases are not as well estimated. For orientation estimates, larger polar angles result in a better yaw estimate, but differences are not significant in pitch and roll. With small beam divergence, errors in orientation have less influence, giving better estimates in altitude. With large divergence, more information is gathered in the x and y directions, improving estimates in those directions. Based on these results, the current beam geometry with a polar angle of  $22.5^\circ$  is a good compromise that avoids the problems introduced by polar angles that are too small or too large.

Next, the effect of possible misalignments on the estimate of the state vector was studied. To accomplish this, several possible misalignments were incorporated. Each of the three LIDAR beams can have misalignments in one or both of two directions. These misalignments are in the polar angle of  $22.5^\circ$  from vertical, and in their clock angle separation of  $120^\circ$  from one another. Additionally, misalignments were also incorporated into the entire beam head assembly. The assembly can have three directional misalignments, effectively a yaw, pitch, and roll, with respect to the spacecraft body frame. For this study, errors of  $\pm 2^\circ$  in any direction were considered the maximum expected alignment error. The study was therefore conducted using the maximum possible misalignment magnitudes in each direction at once. That is, all LIDAR pointing direction errors and head assembly pointer errors were  $\pm 2^\circ$  at the same time. The results of the study are shown in Figure 5.

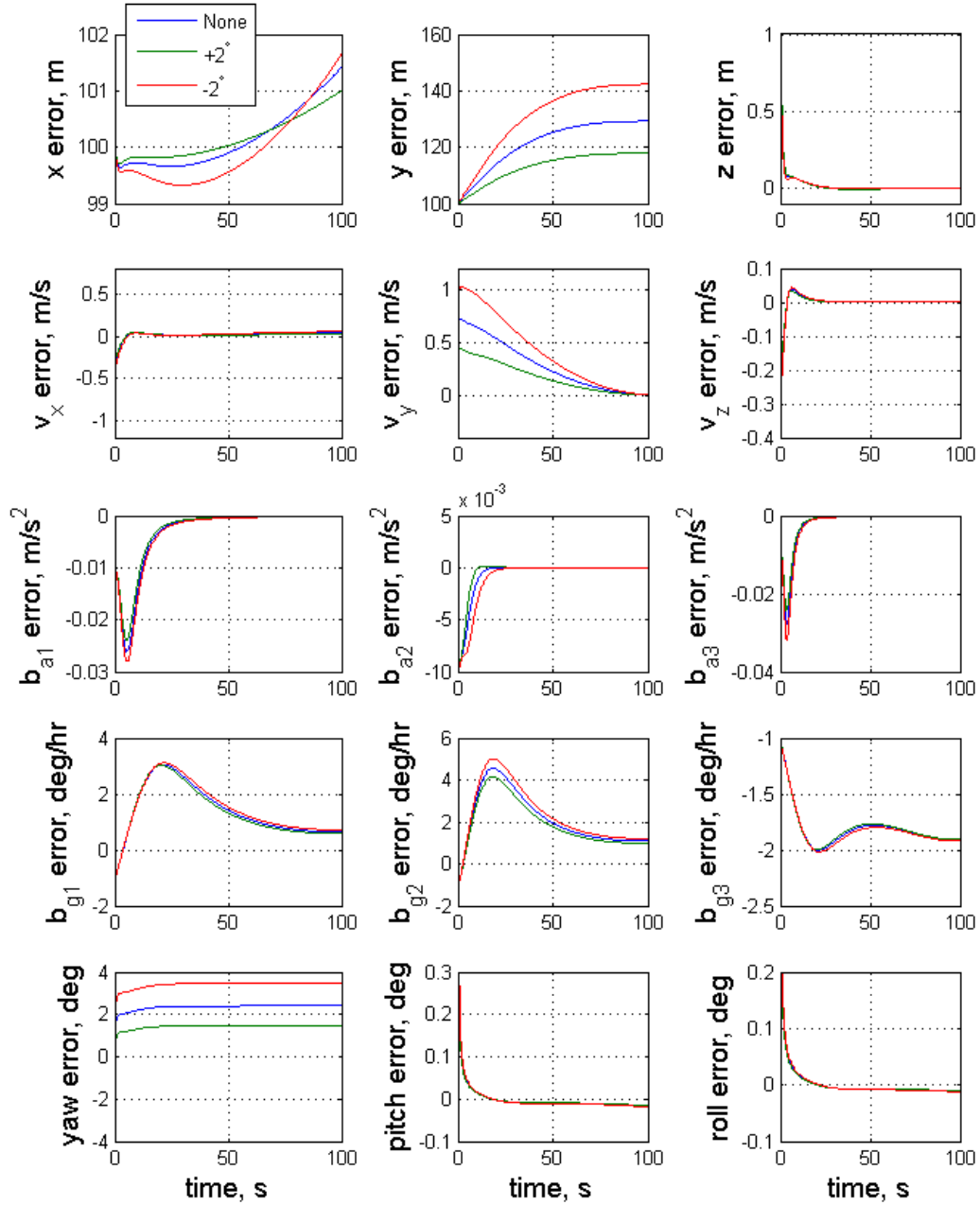


Figure 5. Errors in estimated states for beam and head assembly misalignments.

Even with the maximum possible misalignment errors occurring at the same time, the overall effect of the misalignments is minimal. Estimates of the velocity and

accelerometer and gyro biases are slightly slower to return to the true state, but the magnitude of the error is nearly the same as without misalignments. The effect of the misalignments in the other estimated states is negligible. While other studies with misalignments up to  $10^\circ$  showed significant errors in the estimated states, misalignments of that magnitude are unlikely in this system. Misalignments on the order of  $2^\circ$  as in this study would not be likely to cause significant error in the estimated spacecraft state during application.

Finally, the influence of limited data types was studied. Simulations were run in which only range or only Doppler measurements were used. This was conducted to simulate errors in the data collection which may occur during operations. To accomplish this, the uncertainty of the measurements was drastically increased (15 orders of magnitude), such that the measurements have no effect on the estimate of state. The same trajectory was used, with the standard polar angle of  $22.5^\circ$ . Figure 6 details the state estimate errors for these simulations.

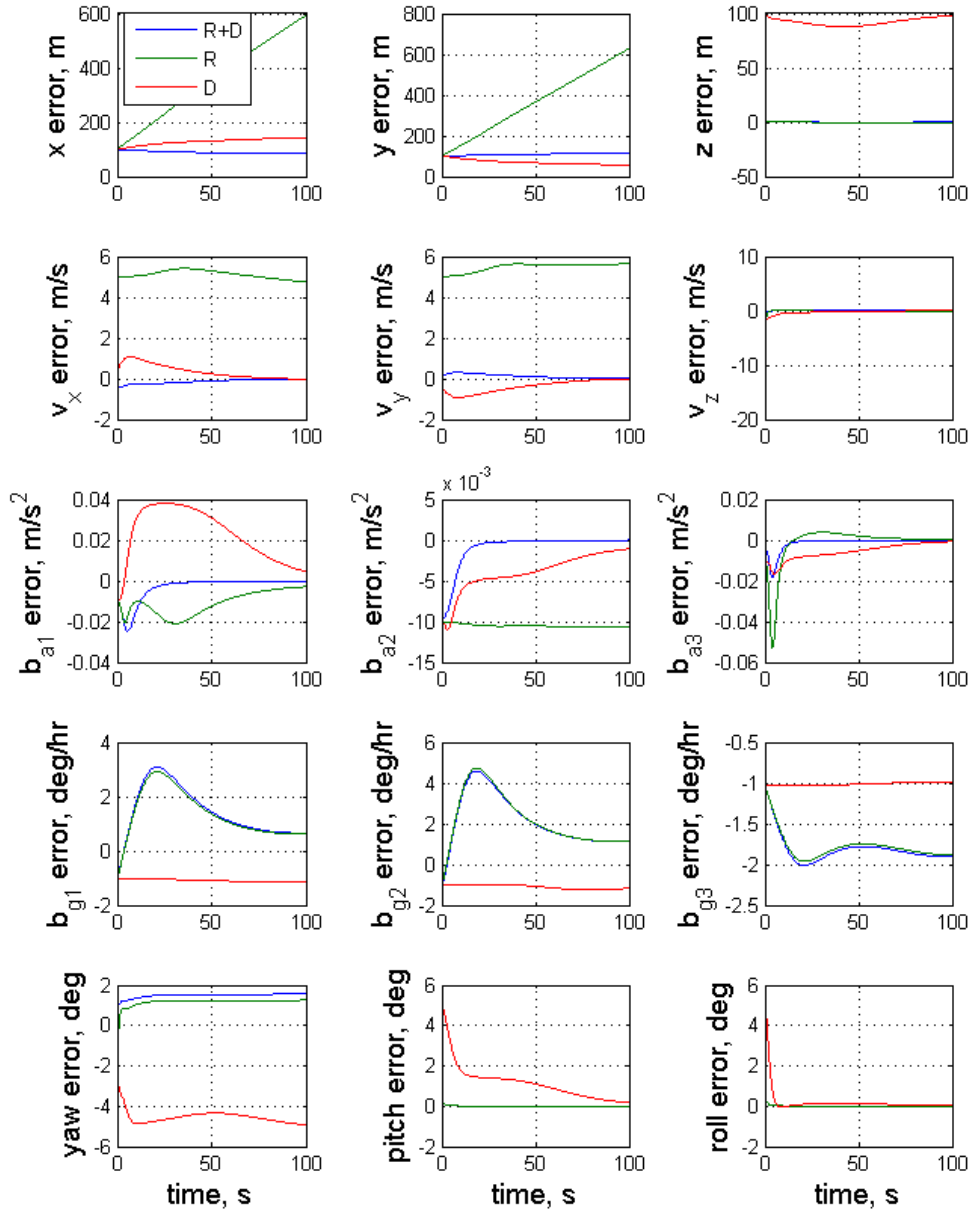


Figure 6. Errors in estimated states for limited data types.

The results of the study indicate that, as expected, having measurements of both range and Doppler provides the best estimate of the state as opposed to having only one type. For the range only case, the altitude and vertical velocity are well determined, as is

orientation. However, all other estimated states suffer significantly. For the Doppler only case, velocities are better estimated than with range. This is expected, as the Doppler measures line of sight velocity, which feeds into the estimate of the spacecraft velocity. However, altitude, orientation, and biases cannot be well estimated with Doppler only. This shows that range measurements provide better estimates of geometrically-determined quantities such as altitude and orientation, while Doppler measurements provide better estimates of velocity. The inclusion of both data types provides the advantages of both, leading to the best possible estimate of the spacecraft state.

### 3 Bumpy Terrains

The filter was then tested by running simulated trajectories over a flat surface with randomly scattered obstacles, simulating rocks on the surface of a planet. To this end, it was necessary to create a system to generate sample terrains for testing. A terrain shaped as a flat surface with various hemispherical bumps was selected as the standard. With a user-defined rectangular area to represent the surface, as well as a total number and an average radius of the bumps, the surface is created by scattering the hemispheres randomly across the surface. A topography array is generated to define the flat surface. For each bump to be placed, a smaller array is defined based on the radius of the bump. This is then placed into the larger topography array at the x and y values corresponding to the center of the bump. In this way, a single large altitude map is generated through the overlay of a number of smaller maps.

Next, these terrains are used to generate the LIDAR measurements that would occur for a spacecraft flying over them. This was accomplished by deriving an exact

formula to represent the intersection of the LIDAR beam with the hemispherical bumps. Note that only the LIDAR range measurements are affected by terrain; the Doppler measurements are not influenced by topography. The surface of each bump can of course be represented as  $(x - x_b)^2 + (y - y_b)^2 + (z)^2 = R^2$ , where  $x_b$ , and  $y_b$  represent the x and y coordinates of the bump center, and R is the radius. Additionally, the xyz location of the end of the beam can be represented as a function of the range coordinate, s, as

$$x(s) = x_0 + \alpha s, \quad y(s) = y_0 + \beta s, \quad z(s) = z_0 + \gamma s$$

where  $(x_0, y_0, z_0)$  is the origin of the beam on the spacecraft, and  $\alpha$ ,  $\beta$ , and  $\gamma$  are the x, y, and z direction cosines of the beam, respectively. Thus, the range measurement value s at which a LIDAR beam impacts the surface of a bump can be calculated by solving the following equation:

$$(x_0 + \alpha s - x_b)^2 + (y_0 + \beta s - y_b)^2 + (z_0 + \gamma s - z_b)^2 - R^2 = 0$$

To calculate the range measurement, the position and orientation of the spacecraft, as well as the location and size of the bump are needed. At each sample point in the simulation, the range measurement of each beam to each of the bumps is calculated. The above equation does not take into account that the object in question is a hemisphere on a flat surface; only a sphere is defined. Thus, additional logic is required for the number of different outcomes of this calculation.

The first and most common outcome is that the beam and the surface of the bump do not intersect, and there is no real solution for s. In this case, the flat surface range measurement is generated. Second, the beam may just touch tangent to the surface, giving only a single range measurement. Third, the beam may travel through the interior of the sphere, passing through the surface twice. In this case, the smaller value of the range

coordinate  $s$ , corresponding to the first intersection with the sphere, is the desired range measurement. However, for cases 2 and 3 above, it is possible that the beam may intersect the surface of the sphere on the bottom half, below the flat surface, which is not a valid solution for the actual terrain. In this case, the flat surface range measurement is then generated.

These range measurements from the simulated bumpy terrain are used as pseudomeasurements in the filter to estimate the state of the spacecraft. The coordinate system and trajectory are identical to that used in the flat surface studies detailed in Section 2. For this simulation, the initial estimate of the state was chosen to be the state used to generate the simulated data. Figure 7, below, shows an overhead view of the trajectory and terrain. The hemispherical bumps scattered across the surface are visible. The variation in size can be seen from the diameter and color of each bump (red indicating a larger bump).

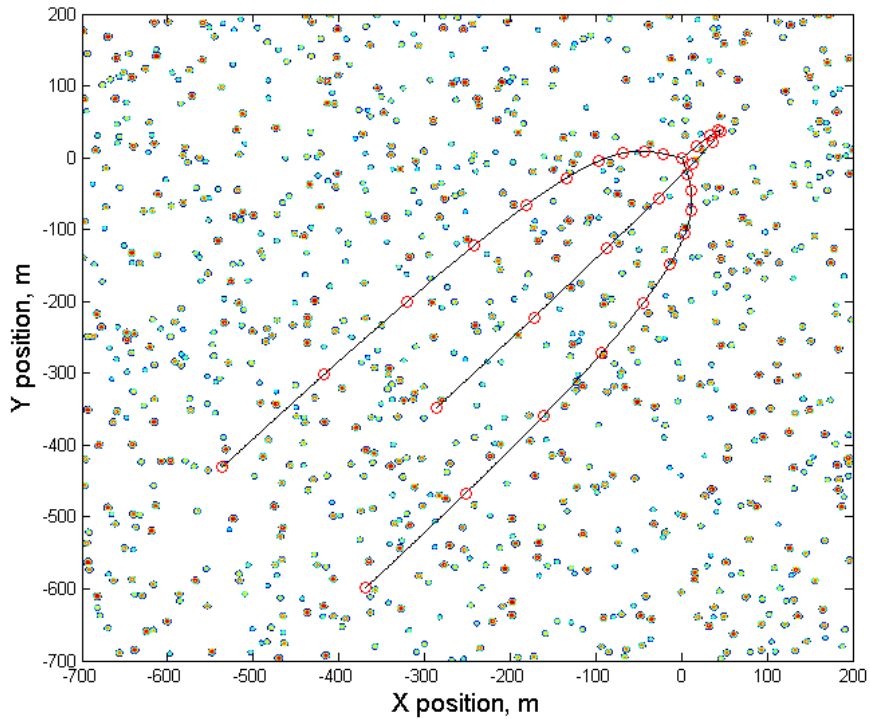


Figure 7. Simulated trajectory over bumpy terrain.

Initial simulations over the terrains with the original filter parameters quickly showed that retuning of the filter was necessary. Figures 8 through 12 show the results of a simulated landing trajectory over a bumpy terrain, using the original filter parameters. In this simulation, the flat surface is populated with bumps of an average height of 3.5m. For each plot, the top row shows the true and estimated state, as well as the uncertainty in the state presented as bounds. The bottom row shows in closer detail the error between the true and estimated state. Figure 8 shows that, for the original filter tuning, large errors in x and y location (on the order of 100 meters) are introduced due to the terrain. These states cannot be estimated for a flat surface, so any errors that are introduced cannot be corrected. The altitude, however, is well estimated by the filter. The influence of the terrain on the estimate is clearly visible, and altitude errors are on the order of 0.5 m.

The reason for the large deviation in x and y position becomes clear in Figure 9. The x and y velocities have errors on the order of 5 m/s due to the influence of the terrain. These errors are primarily due to the errors in estimated orientation, which cause the Doppler measurements to feed into the velocity estimate differently. The estimated velocities do return to the true state, but very slowly. The errors in estimated velocity feed into the position estimate, so the larger the error in velocity, the faster the error in position will grow. Again, the z component is the most easily estimated quantity; errors are on the order of 0.1 m/s, and the influence of the terrain is clearly visible.

Figures 10 and 11 show the IMU bias estimates. Here, the subscripts x, y, and z denote the roll, pitch, and yaw axes of the body, respectively. Figure 10 shows that all three accelerometer bias estimates are affected, but measurements help to correct the errors. The roll and yaw directions are affected by similar amounts, and both return to the true state. The bias estimate in the pitch direction does not settle back to the true state. However, the error is an order of magnitude smaller than those in the roll and yaw directions. In Figure 11, the influence of the terrain on the gyro bias estimates is clear. Each time a beam tracks over a bump, the estimate of the bias jumps. This is because the shortened range measurement can be corrected by, among other things, an orientation change to adjust the lengths of each beam. However, orientation changes due to the terrain are not desirable, as they are not actually occurring in the trajectory. The instantaneous changes in the orientation estimate that could result are of course impossible, as a rigid body cannot change orientation instantaneously. Instead, more of the error is shifted into the gyro bias estimates. Each of the estimates begins to correct after a beam tracks over a bump, but the estimate becomes worse each time a LIDAR

beam tracks over a bump. Note that errors in the pitch and roll directions are significantly higher than in the yaw direction. This can be interpreted more easily when Figure 11 is examined with Figure 12, showing the estimated orientation. Errors in pitch and roll are small, due to most of the error being absorbed in the gyro bias. However, the yaw, which cannot be estimated for a flat surface, has a very large error, because yaw changes do not affect the range measurements very much for a flat surface. That is, for a vehicle that is not pitched or rolled above the flat surface, the range measurements are the same for any angle of yaw.

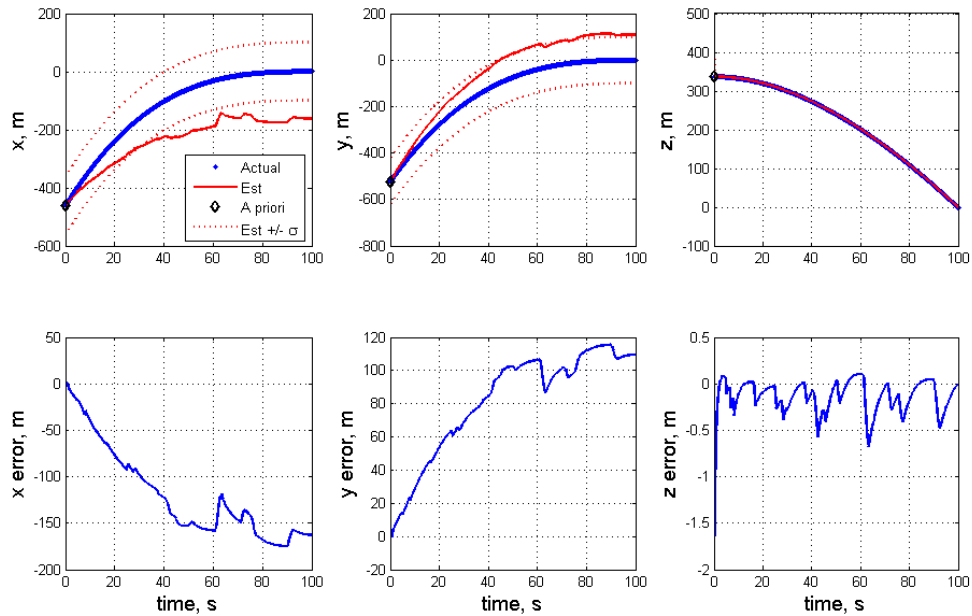


Figure 8. Position estimate and error versus time with original filter parameters.

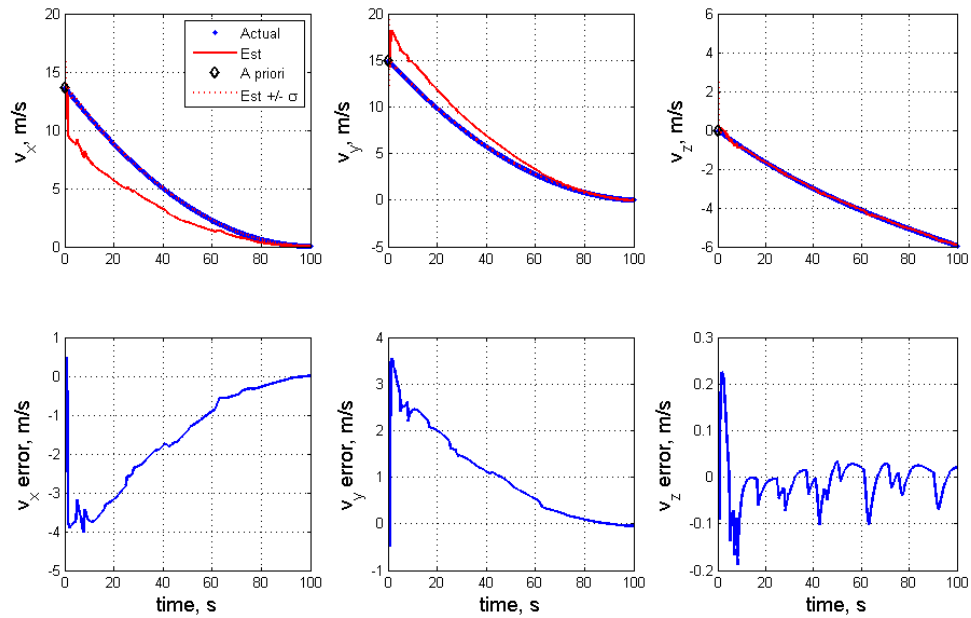


Figure 9. Velocity estimate and error versus time with original filter parameters.

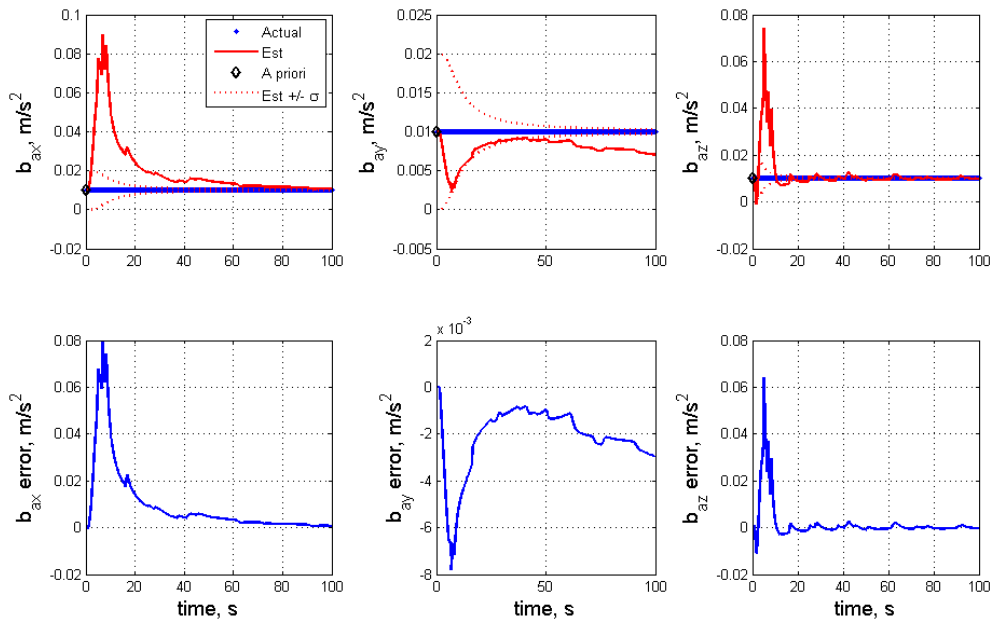


Figure 10. Accelerometer bias estimate and error versus time with original filter parameters.

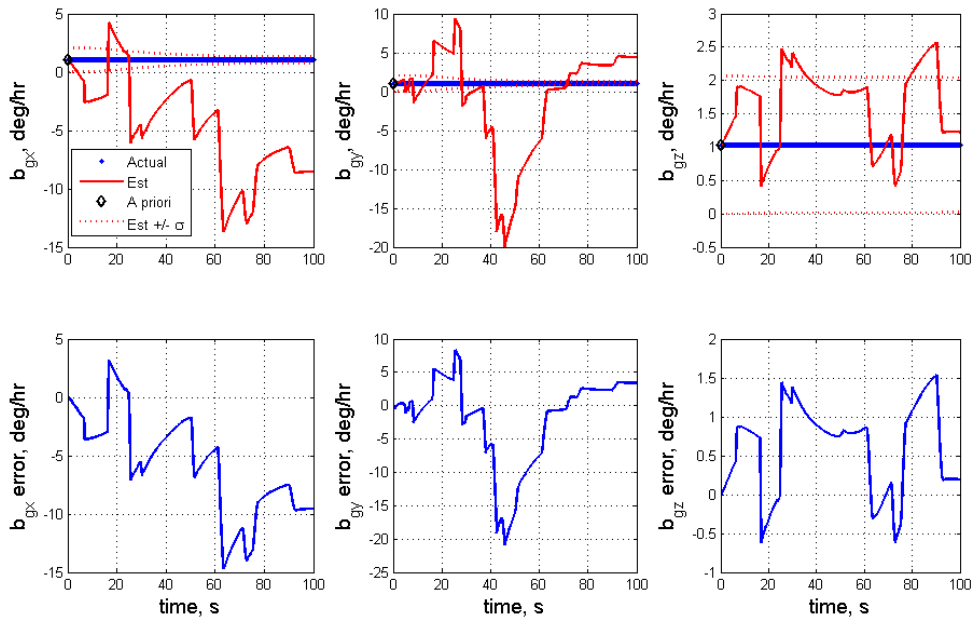


Figure 11. Gyro bias estimate and error versus time with original filter parameters.

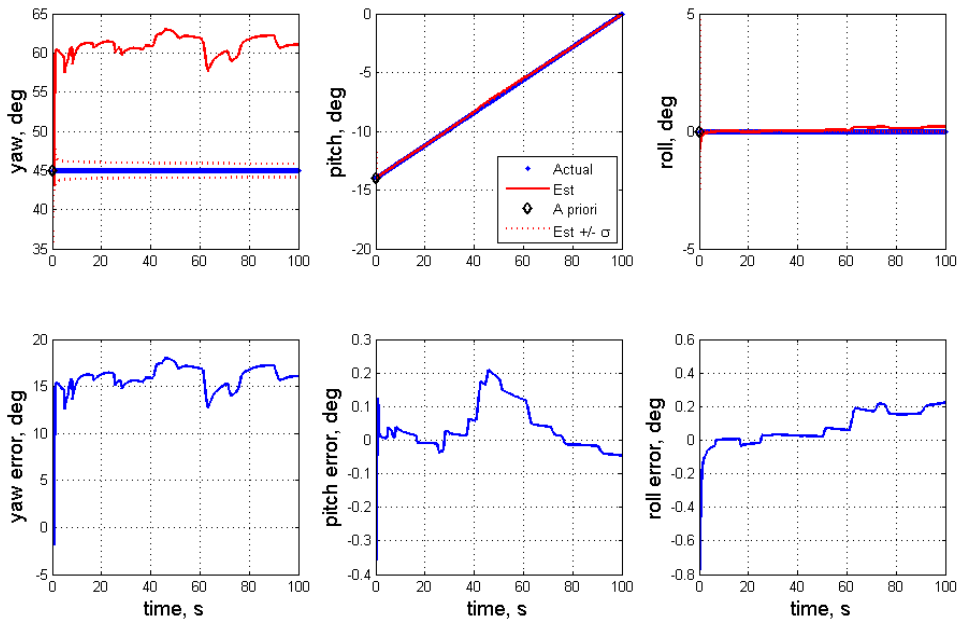


Figure 12. Orientation estimate and error versus time with original filter parameters.

To reduce the influence of the terrain on the estimated states of the spacecraft, numerous methods of tuning the filter were examined. These included intervention analysis, in which range measurements that deviated greatly from the previous measurement would not be fed into the filter at all. Ultimately, the method chosen to tune the filter was changing the uncertainty of the range measurements and the initial estimate of state covariance. What was selected was increasing the LIDAR range measurement uncertainty to levels near the height of the terrain, so that the bumps will have less influence on the estimated states. By tightening the initial orientation covariance, the filter will further resist changes in orientation due to the terrain. This will keep orientation changes from causing larger errors in the velocity estimate. The changes in the filter parameters are detailed in Table 1, below. Note that these new parameters are used in the filter for the rest of the results presented in this document. Figures 13 through 17 show the effect of this filter tuning in reducing the influence of the terrain, for the same trajectory and terrain as the above results in Figures 8 through 12.

Errors in the x and y position are reduced by two orders of magnitude, from 100m to 1m. Error in the altitude estimate is also reduced by approximately 50%. Velocity estimates are also reduced by several orders of magnitude, as are those for both the accelerometer and gyro IMU biases. The more accurate the velocity estimates are, of course, the main driver in producing the more accurate position estimates. In orientation, the pitch and roll errors are also further reduced from their already small values. The yaw estimate is far less affected by the terrain than with the original filter parameters. By retuning the filter in this manner, the influence of the terrain on the estimated states through the range measurements is greatly reduced.

**Table 1. Adjusted Filter Parameters**

	Initial state covariance		Beam	Range measurement uncertainty	
	Original	Retuned		Original	Retuned
Position – x	100 m	100 m	1	0.1 m	2 m
y	100 m	100 m	2	0.1 m	2 m
z	100 m	100 m	3	0.1 m	2 m
Velocity – u	5 m/s	5 m/s			
v	5 m/s	5 m/s			
w	5 m/s	5 m/s			
Accel. Bias	0.01 m/s <sup>2</sup>	0.01 m/s <sup>2</sup>			
	0.01 m/s <sup>2</sup>	0.01 m/s <sup>2</sup>			
	0.01 m/s <sup>2</sup>	0.01 m/s <sup>2</sup>			
Orientation - Yaw	5°	1°			
Pitch	5°	1°			
Roll	5°	1°			
Gyro bias	5x10 <sup>-6</sup> rad/s	5x10 <sup>-6</sup> rad/s			
	5x10 <sup>-6</sup> rad/s	5x10 <sup>-6</sup> rad/s			
	5x10 <sup>-6</sup> rad/s	5x10 <sup>-6</sup> rad/s			

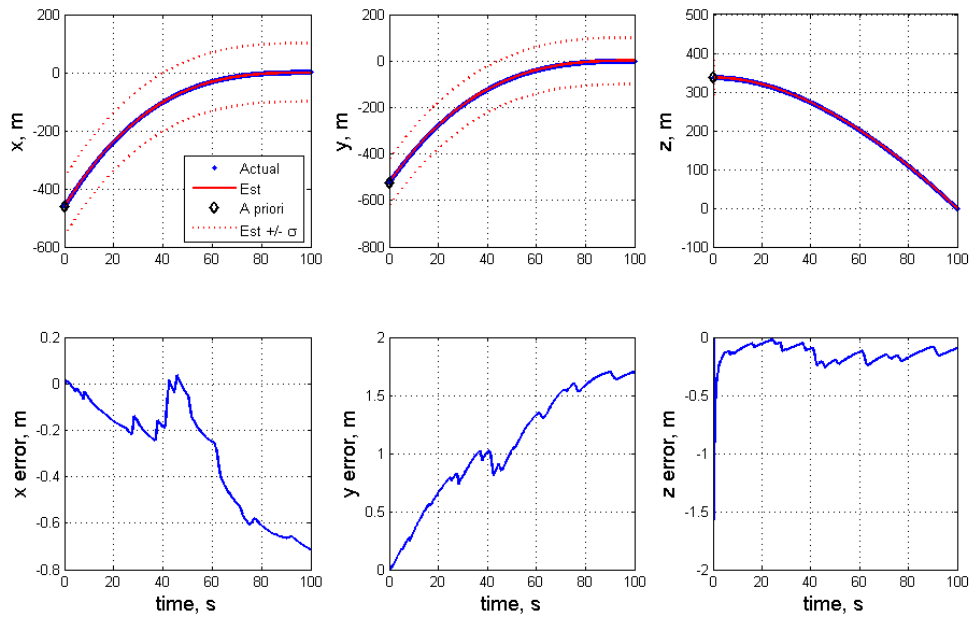


Figure 13. Position estimate and error versus time with new filter parameters.

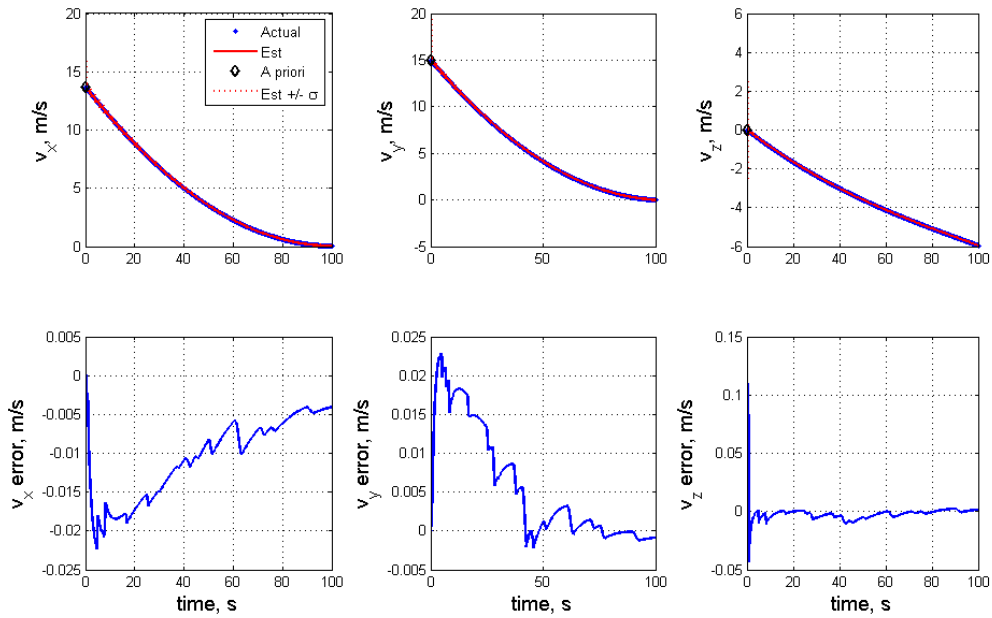


Figure 14. Velocity estimate and error versus time with new filter parameters.

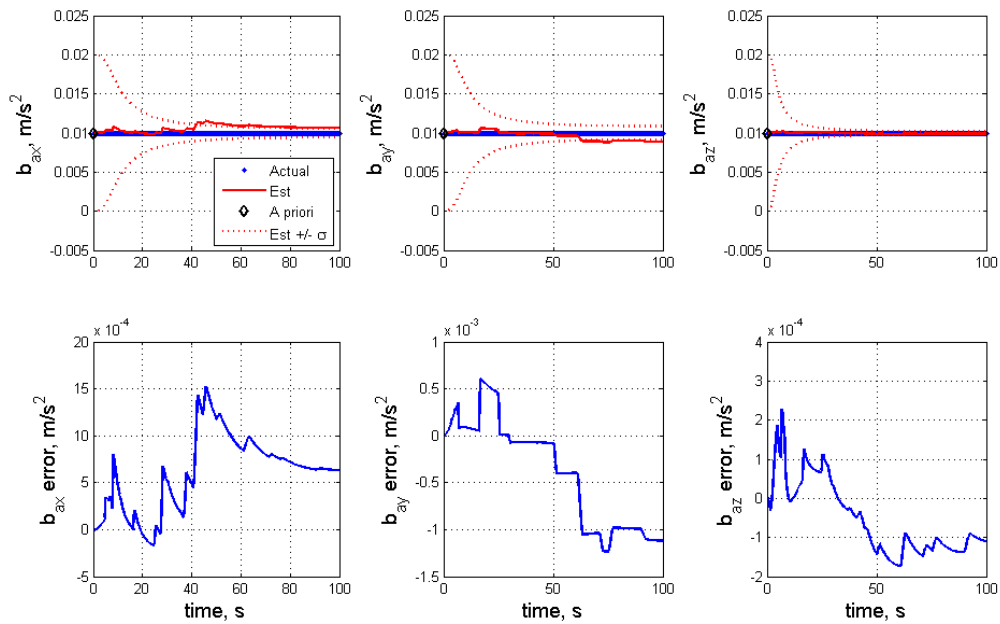


Figure 15. Accelerometer bias estimate and error versus time with new filter parameters.

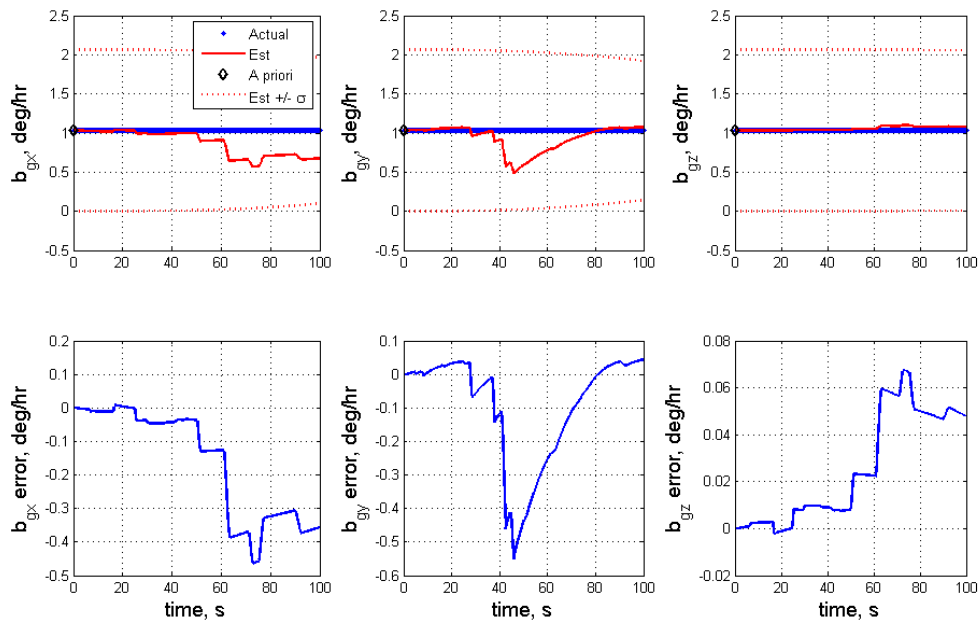


Figure 16. Gyro bias estimate and error versus time with new filter parameters.

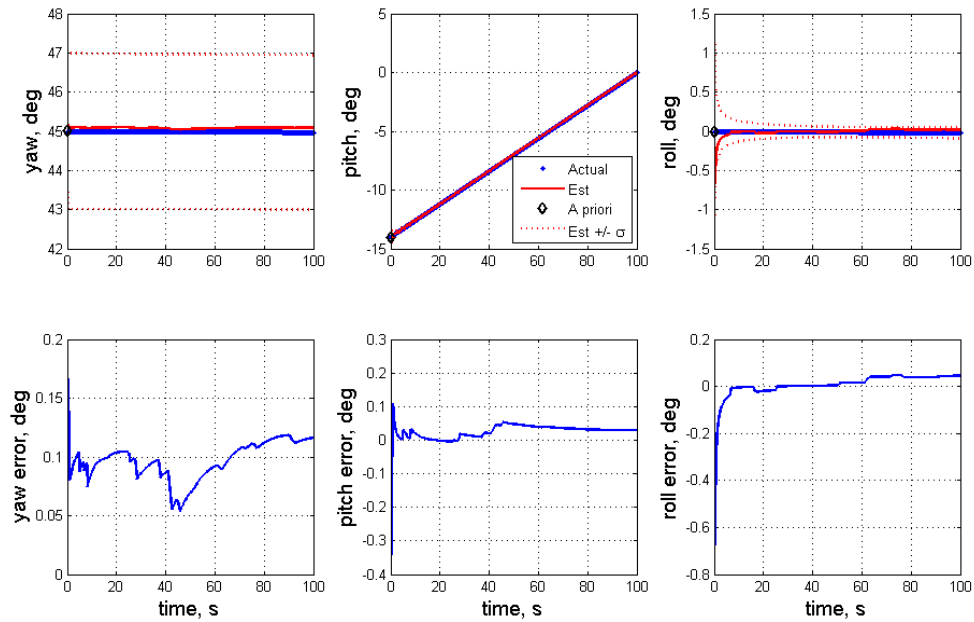


Figure 17. Orientation estimate and error versus time with new filter parameters.

As a separate approach towards filter retuning, an effort was made to separate the LIDAR measurements of range and Doppler to compare with one another and determine terrain so that bumps will not influence the estimate. Because the Doppler measurements are unaffected by the terrain, if the range measurements could be determined from Doppler, any differences in the calculated and measured range would have to be due to the terrain. To this end, a method was developed to calculate range measurements at the current time step based on the previous estimated state, and the accelerometer and Doppler measurements. Because the Doppler measurements are line-of-sight velocity measurements, the velocity vector of the spacecraft can be determined from simple geometry. With this velocity and the previous estimated position, the current position of the spacecraft can be determined using a  $x_2 = x_1 + v_1 \Delta t + g \Delta t^2$  approximation, where the

subscripts 1 and 2 represent the state at times before and after  $\Delta t$ , respectively. In addition, the orientation can be estimated using a  $yp_r_2 = yp_r_1 + \omega_m \Delta t$  approximation. With this new position and orientation, the range measurements that would be expected assuming a flat surface are generated. These calculated measurements are then compared to the actual range measurements. Differences between the two sets of measurements are then due to terrain. Figure 18 shows the difference between the range measurements seen over the flat surface and the bumpy surface, both the actual and those calculated from the Doppler measurements.

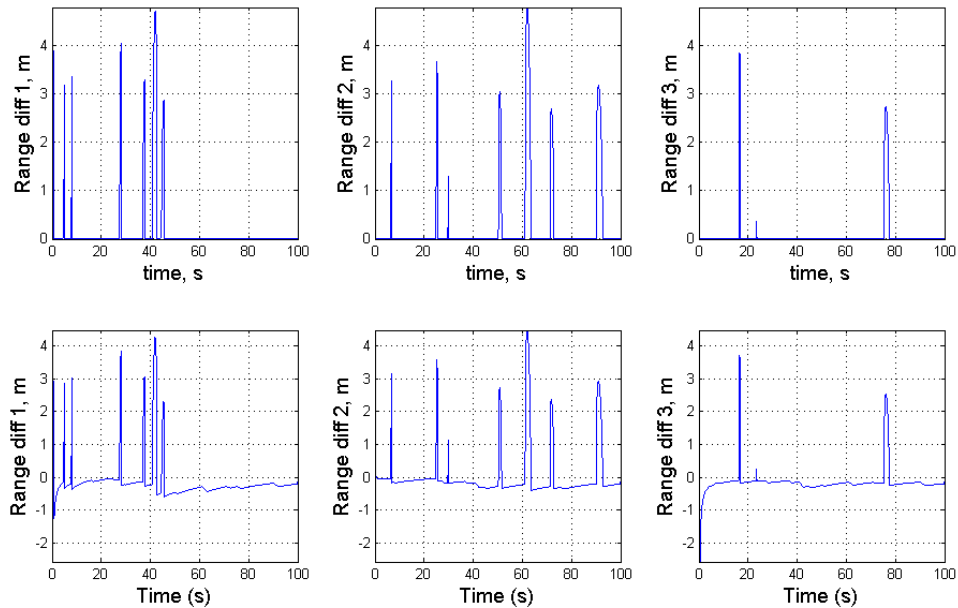


Figure 18. Range measurement differences between true surface and assumed flat surface, actual (top) and Doppler-derived estimation (bottom).

While imprecise due to approximations made in the derivation, this method shows some promise towards determining when a LIDAR beam impacts a bump using the Doppler measurements, which do not change due to the terrain. The difference between

measurements should be zero at all times except when tracking over a bump. However, because the estimated state from the filter is used to calculate the predicted range measurements, the errors in the estimate drive the difference from zero. Despite the limitation, this method does allow for the determination of the terrain, without using the range measurements. A possible application of this method is to inflate the uncertainty in the range measurements only when a beam is tracking over a bump, and lowering it when tracking over a flat surface. This should allow a greater accuracy in the estimated states. This method has not been pursued beyond this point, but is a possible subject of interest for further research.

## 4 Washboard Terrains

The filter was tested by running simulated trajectories over a washboard surface, to simulate hilly terrain. This was accomplished by generating pseudo-observations over a sinusoidal surface, defined by  $z = h_t \sin(2\pi(x - x_0) / \lambda_t)$ , where  $h_t$  is the height of the terrain,  $\lambda_t$  is the wavelength of the terrain in meters,  $x$  is the spacecraft current position in  $x$ , and  $x_0$  is the spacecraft original position in  $x$ . Thus, the shape of the terrain is defined based only on  $x$ , and is constant for all  $y$  at any  $x$ . Figure 19 shows an example of such a terrain. By simulating long duration steady level flight over this terrain, the steady-state response of the filter to the terrain was analyzed.

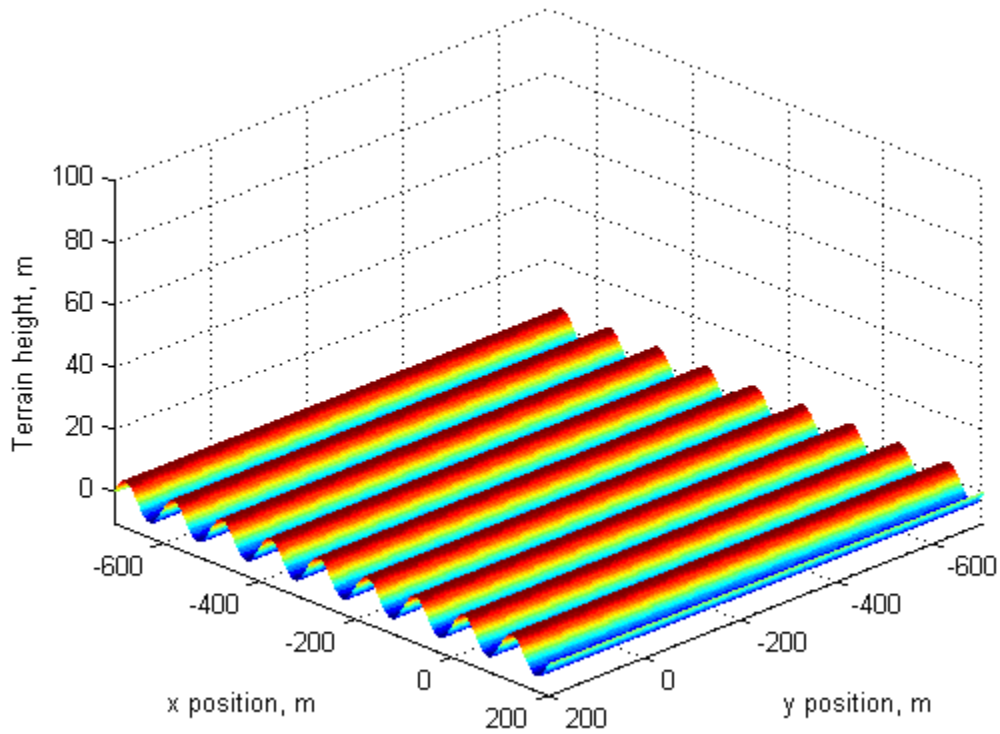


Figure 19. Sample washboard terrain, 5m amplitude by 100m wavelength.

First, the effect of terrain height on the estimated position was studied. Due to the constant horizontal velocity of the spacecraft, the LIDAR range and Doppler signals have an induced frequency of  $\frac{u_{sc}}{\lambda_t}$ . The altitude gain, defined as the ratio of the steady-state oscillation in the altitude estimate to the terrain height, was determined. The gain was then calculated over a range of apparent frequencies and a range of terrain heights. In addition, the altitude gain was calculated in each case using both range and Doppler measurements, and only range measurements. The results of this study are shown in Figure 20, for three different levels of terrain height, and the default levels of

accelerometer and gyro state noise. Six tested velocities give six apparent frequency data points.

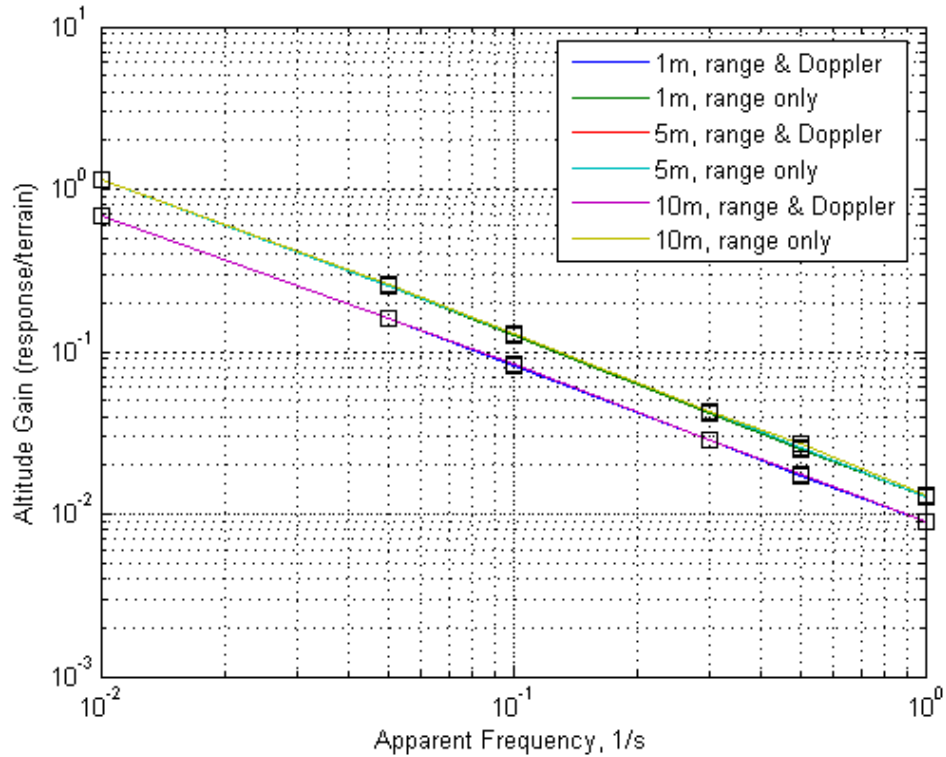


Figure 20. Effect of terrain height on altitude gain, 100m wavelength terrains, 300m altitude.

Figure 20 shows that for a given altitude, there is a clear linear relation between the amplitude of the terrain and the amplitude of the steady-state oscillation in the altitude estimate. As the apparent frequency increases, the altitude gain decreases one decade per decade, so the gain is proportional to one over the apparent frequency. For very low apparent frequencies, the gain can exceed 1. That is, the oscillation in the altitude estimate exceeds the height of the terrain. The gain should approach 1 as the apparent frequency approaches zero. When the gain is 1, the spacecraft is exactly following the

terrain. However, due to the influence of the filter on all the estimated states, the gain slightly exceeds 1. The gain is effectively the same for any terrain amplitude between 1 and 10 meters. While an increase in the amplitude of the terrain will produce a greater oscillation in the altitude estimate, the ratio of the quantities remains constant. The linear relation also holds for the simulations in which only range measurements are used. The range-only cases result in larger gains, as the Doppler measurements are not available to help correct the velocity estimates, which would constrain altitude deviations. These results may be accurate only within this linear region.

The response of course depends on the state noise levels, so it is of interest to vary them and study the effects. By testing the same trajectory with varying accelerometer and gyro state noise levels, the effect of the state noise on the gain was determined. The state noise levels on the accelerometers and gyros were increased and decreased from the standard case by a factor of 10. Figure 21 shows a similar altitude gain plot detailing results obtained.

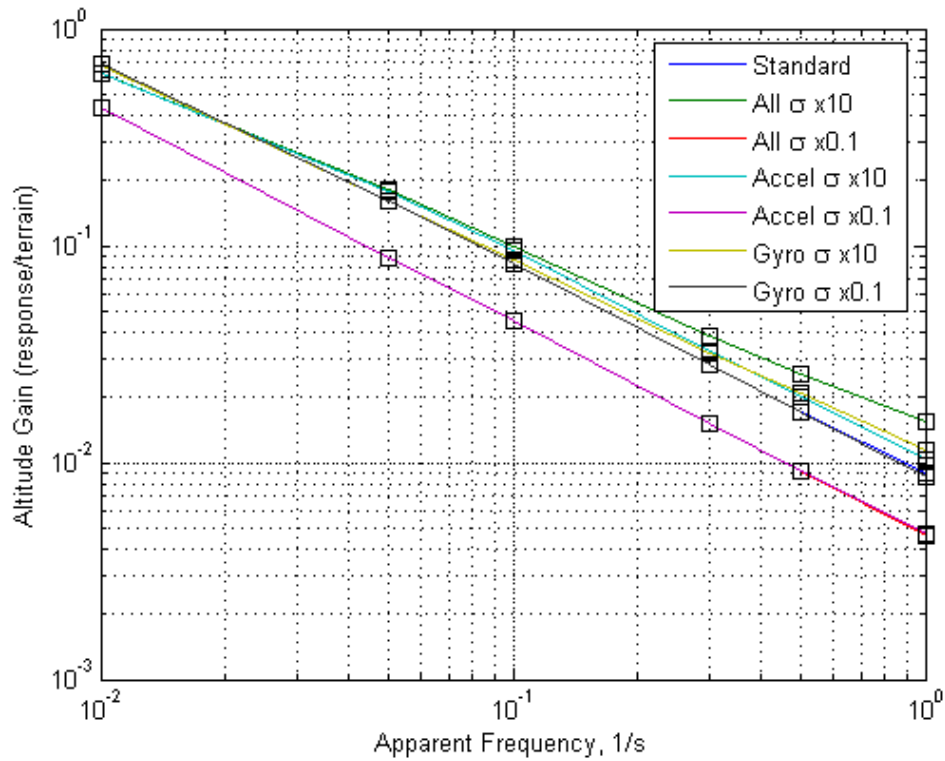


Figure 21. Effect of state noise on altitude gain, 1m by 100m terrain, 300m altitude.

The general trend of the gain decreasing with increasing apparent frequency is still clear. By increasing or decreasing the state noise levels of the accelerometers, gyros, or both by an order of magnitude, their effect on the altitude gain became evident. When only the accelerometer sigma is increased by a factor of 10, the slope is smaller because with less confidence in the IMU data, the LIDAR is relied upon more heavily. This works well at low frequencies where the range measurements change slowly, but not as well at high frequencies. Increasing all sigmas by a factor of 10 produces a similar change, but increasing only the sigma on the gyros causes little change in the gain. Thus, the gyro state noise has little effect on the altitude gain. Decreasing all sigmas reduces all gains, because there is more confidence in the IMU data, and the filter does not allow the

LIDAR range measurements to affect the altitude estimate as much. This is again mainly due to the accelerometer sigma, as the decreased accelerometer sigma is nearly the same. Again the gyro sigma change has little effect on the gain. It appears that the filter is much more sensitive to changes in the accelerometer state noise than to changes in the gyro state noise. It may seem preferable to continue decreasing the state noise further to decrease the altitude gain. However, as the altitude estimate is improved, other estimated states are worsened. A method of tuning the state noise based on some knowledge of the velocity and apparent frequency to minimize the altitude gain is a topic of further interest.

Next, the effect of the spacecraft altitude on the altitude gain was studied. Over the same range of apparent frequencies, the altitude of the spacecraft was varied between 200 and 400 meters. The results of simulations are shown in Figure 22, below.

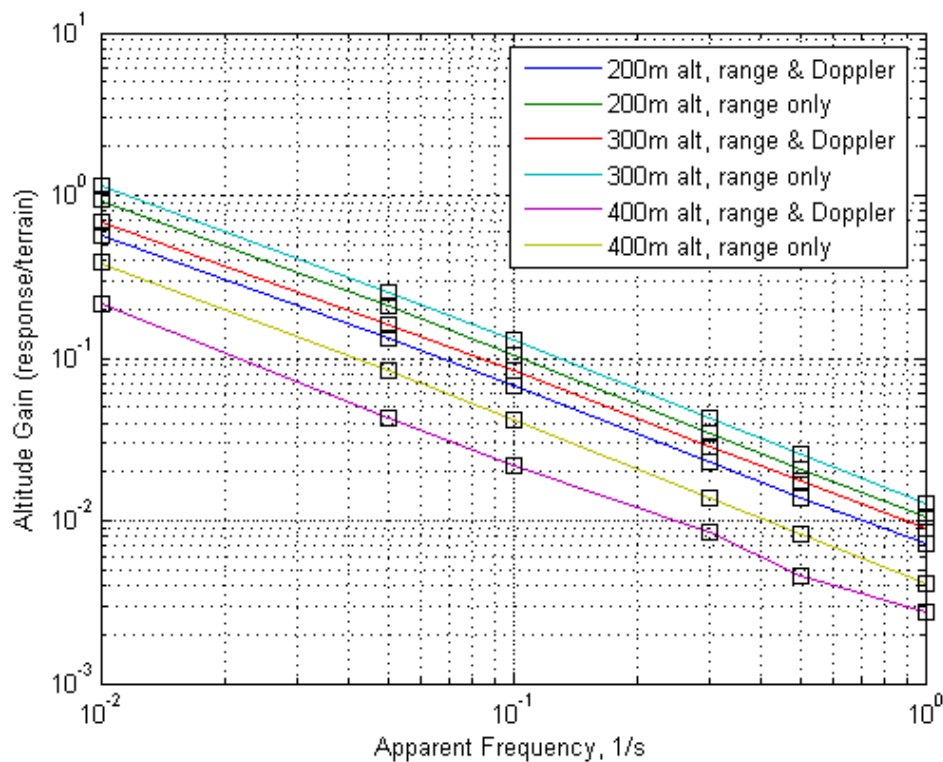


Figure 22. Effect of spacecraft altitude on altitude gain, 5m x 100m terrain.

The same pattern of decreasing gain with increasing frequency is again evident, as is the shift in the curves due to the inclusion or exclusion of Doppler measurements. Because the Doppler measurements affect the position estimate through velocity, the “range only” gains will always be larger than the corresponding case including Doppler measurements. There is also a clear effect of the spacecraft altitude on the gain. Changes in the altitude result in effective upward or downward shifts of the gain curve. Note that increasing the spacecraft altitude from 200 to 300 m increases the gain, while increasing from 300 to 400 m decreases it. This seemingly contradictory result is due to the geometry of the LIDAR beams and terrain. A main factor in this phenomenon is the phase difference between the forward (1) and rear (2 & 3) LIDAR beams, which became an area of interest for further research.

The spacecraft altitude and footprint in the x-direction can be described through the following relation:  $footprint = (altitude) \sin(a)(1 - \cos(\mu))$ . For a given trajectory, the footprint was varied between and 45 and 720 degrees. For a 360 degree width footprint, the footprint is the same length as the terrain wavelength, and scales linearly. To accomplish this, the altitude was varied according to the above relation. Figure 23, below, shows the resulting altitude gain.

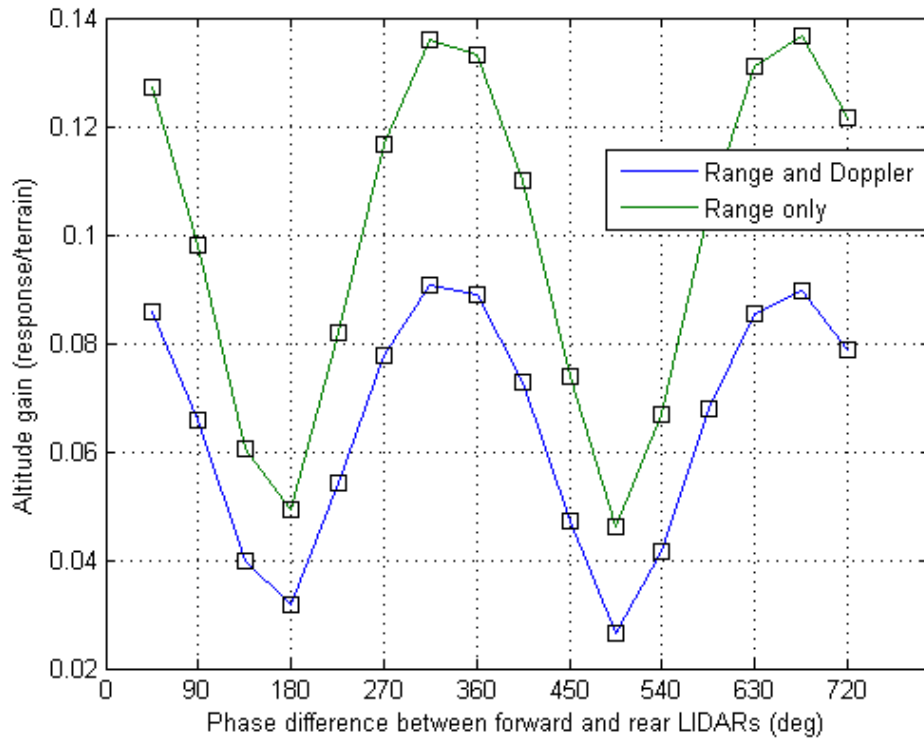


Figure 23. Effect of LIDAR phase difference on altitude gain, 1m x 100m terrain, 10 m/s.

The altitude gain, rather than steadily increasing or decreasing with increasing altitude, fluctuates according to the phase difference between the forward and rear LIDAR beams. The gain follows a similar pattern whether the Doppler measurements are included with the range measurements or not. Again, in the range only case, the altitude gain is larger. That is, the estimated altitude changes a greater amount, due to the decrease in available information caused by the lack of Doppler measurements. Note that the minimum gain occurs at 180 degrees, while the maximum occurs at 360 degrees. The reason for the shift that causes the minimum and maximum not to occur at 540 and 720 degrees is lag caused by the geometry of the beams and the increased altitude. Of further

interest were the responses of the accelerometer, gyro, and pitch in these cases, which are shown in Figures 24 through 26.

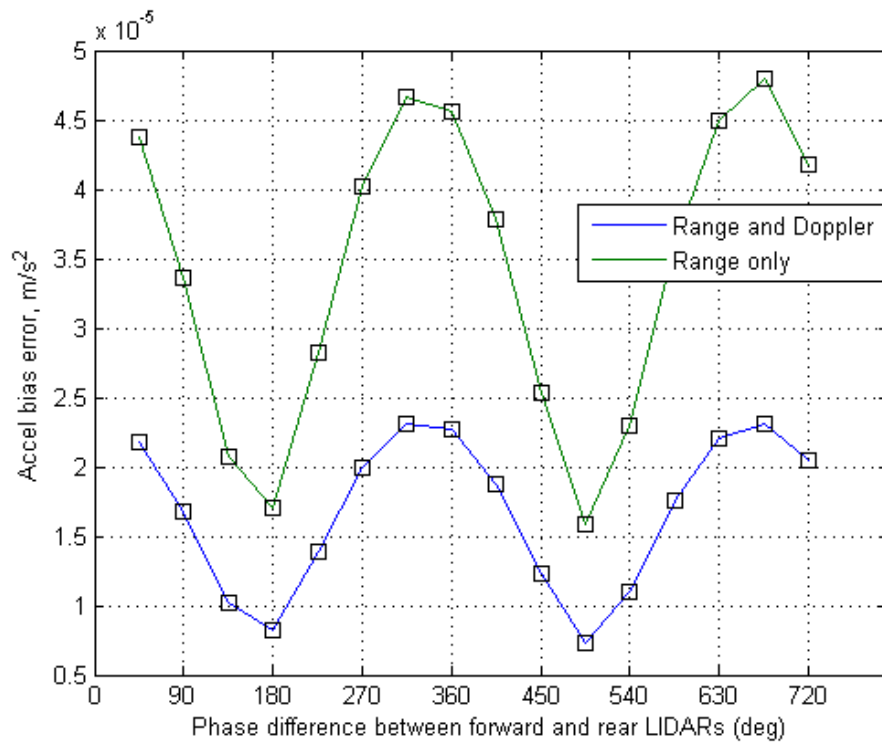


Figure 24. Steady-state z-accelerometer bias error, 1m x 100m terrain, 10 m/s.

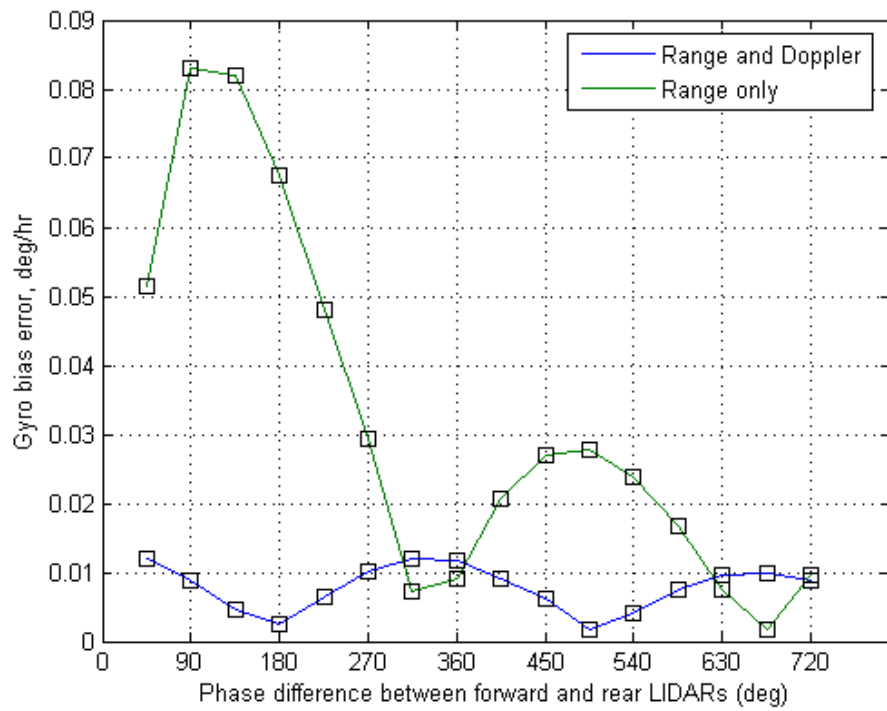


Figure 25. Steady-state y-gyro bias error, 1m x 100m terrain, 10 m/s.

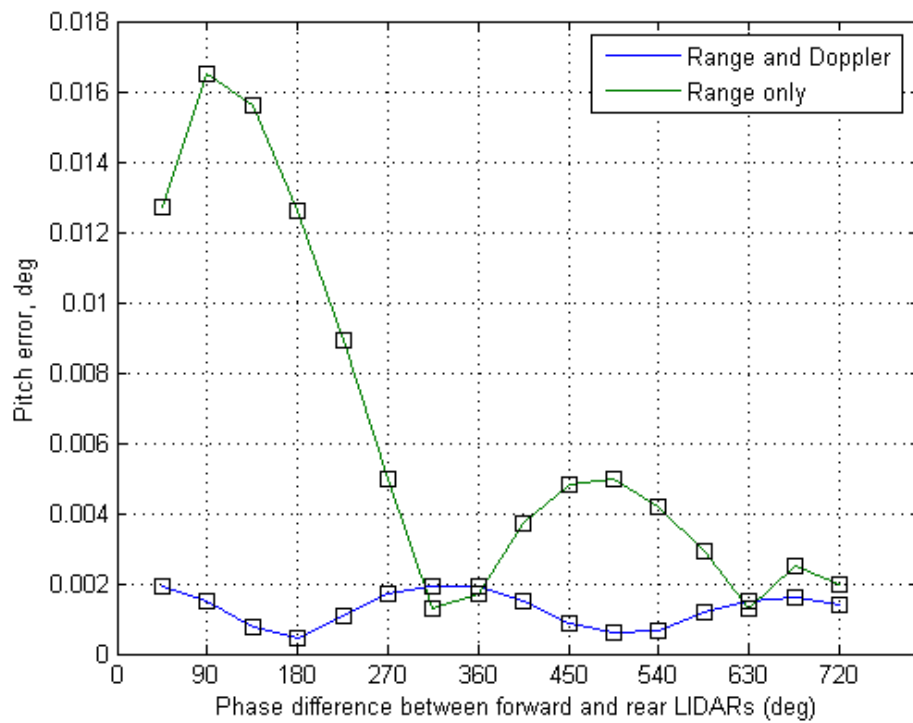


Figure 26. Steady-state pitch error, 1m x 100m terrain, 10 m/s.

In all three estimated states, the case using both range and Doppler measurements exhibits a clear pattern of oscillation with changing phase difference, and a consistent amplitude. The accelerometer bias oscillation is similar to the altitude gain oscillation. The minimum and maximum amplitudes occur at 180 and 360 degrees, and the range only case has greater amplitude due to the decrease in the available information. However, the gyro and pitch estimates display a much different behavior. Rather than the range only case having a similar shape to the range and Doppler case, it instead follows a decaying curve, and is not in phase with the range and Doppler case. The reason for the decreasing amplitude is that for a given change in the range measurement, the pitch change necessary to correct for the change decreases with increasing altitude.

For the range only case, the pitch and gyro have a “worst case” when the LIDAR beams are separated by 180 degrees and its multiples, while the “best case” occurs at 360 degrees and its multiples. At 180 degrees, the range measurement in the forward beam is increasing, while the measurements in the rear two are decreasing. Without the Doppler measurements to aid in correcting the estimated states, this becomes the worst case. Because the slope of the surface is greatest at this phase difference, the estimates are changed the most. At 360 degrees, the forward and rear beams are increasing or decreasing at the same time, resulting in the best case scenario, because the measurement changes can be accomplished through position changes, without significant pitch or gyro bias change.

## 5 Step Terrains

The filter was also tested over a step terrain, simulating a sudden change in the average terrain height. The surface remains flat, with no bumps or other features, but the altitude is increased by a step function. This could simulate a mesa type terrain or a cliff face. The range measurements for this case are generated in the same way as for a flat surface, whether the LIDAR beam is impacting the lower surface in front of the step or the top of the step. The only difference comes when the beam impacts the vertical wall of the step. Range measurements are generated for the flat surface and for the top of the step. At each sample point, based on the ground track of each beam and the location of the step, the proper measurement is selected. If neither of the solutions is valid, the beam must be impacting the vertical face of the step. In this case, the distance to the vertical surface is calculated as the range measurement.

The following results show the influence of the step terrain on the estimate of the spacecraft state. The trajectory is the same as that used in the previous section. However, the surface is flat aside from the step – no other terrain features are present. The height of the step for this case is 1 m. The vertical face of the step is at a  $45^\circ$  angle to the direction of the trajectory. The reason for this orientation of the surface was to study the case that would influence the estimate of the state the most. If the face of the step were perpendicular to the direction of the trajectory, the influence would be minimal. The forward beam would track over the step, shortening the range measurement. Because a flat surface is assumed in the filter, the main effect of this would be a pitch change to correct the range measurement. After the two rear LIDAR beams track over the step as

well, the pitch would correct in the opposite direction, and the overall effect on the estimate will be primarily in pitch. However, when the step is at an angle to the trajectory, the rear beams will not track over the step at the same time. This will cause a change in the estimated roll, as well as pitch. It will also cause an effect on all the estimated states. Figures 27 through 31 show the influence of this step terrain on the estimate.

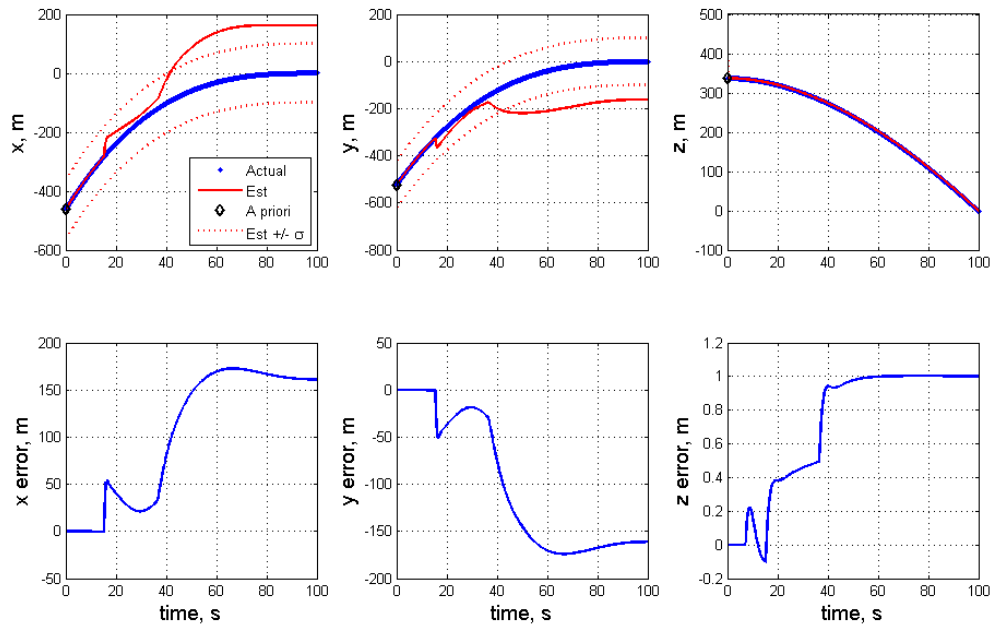


Figure 27. Influence of step terrain on position estimates.

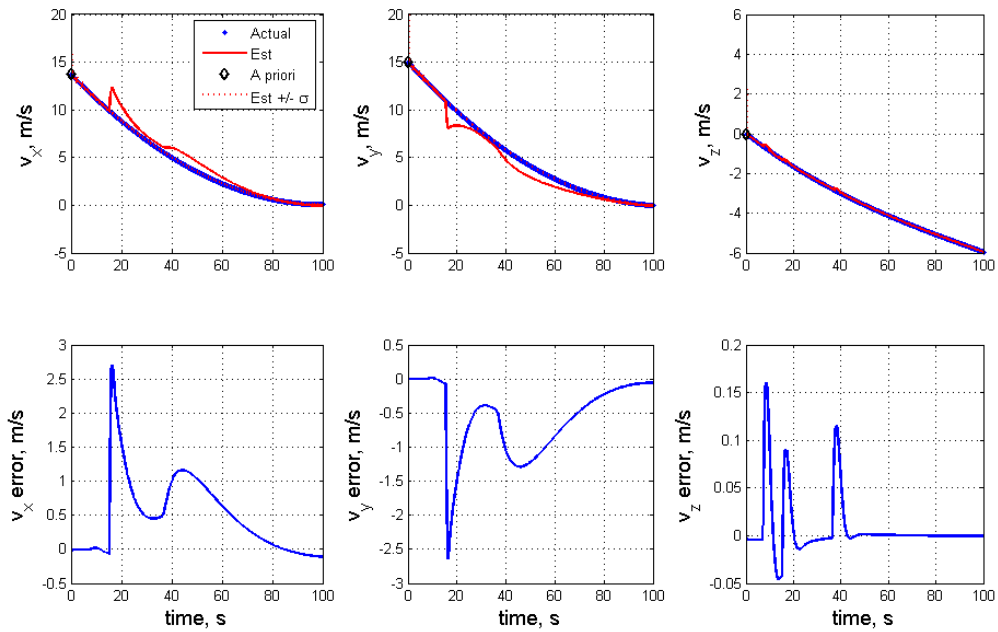


Figure 28. Influence of step terrain on velocity estimates.

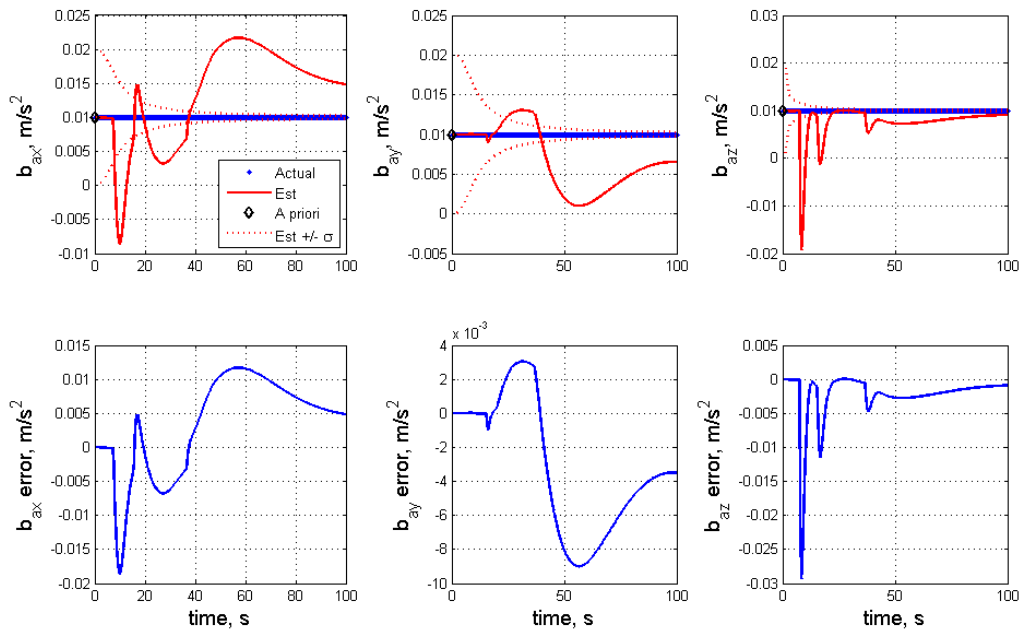


Figure 29. Influence of step terrain on accelerometer bias estimates.

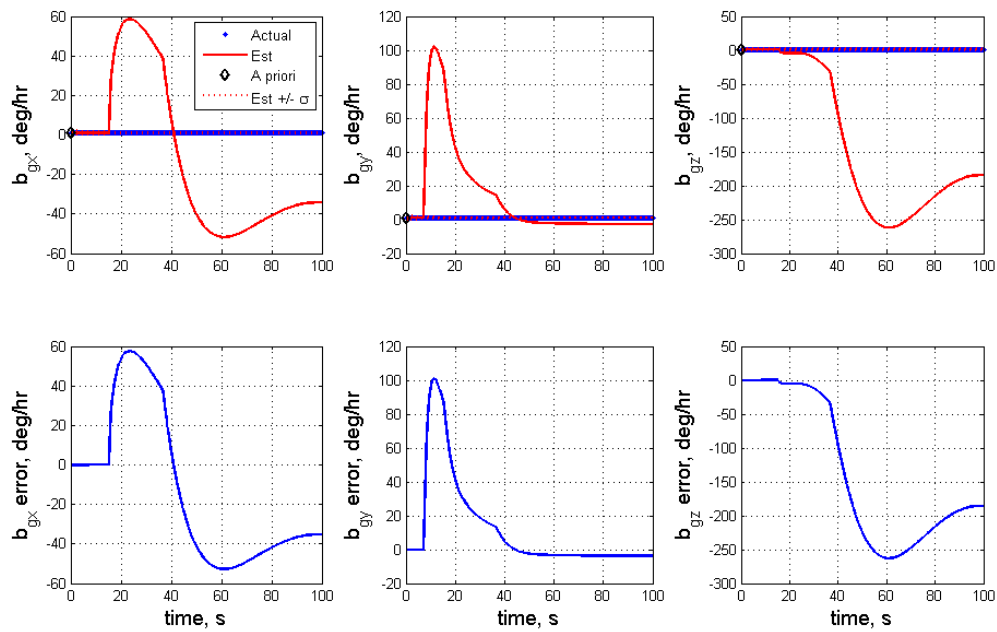


Figure 30. Influence of step terrain on gyro bias estimates.

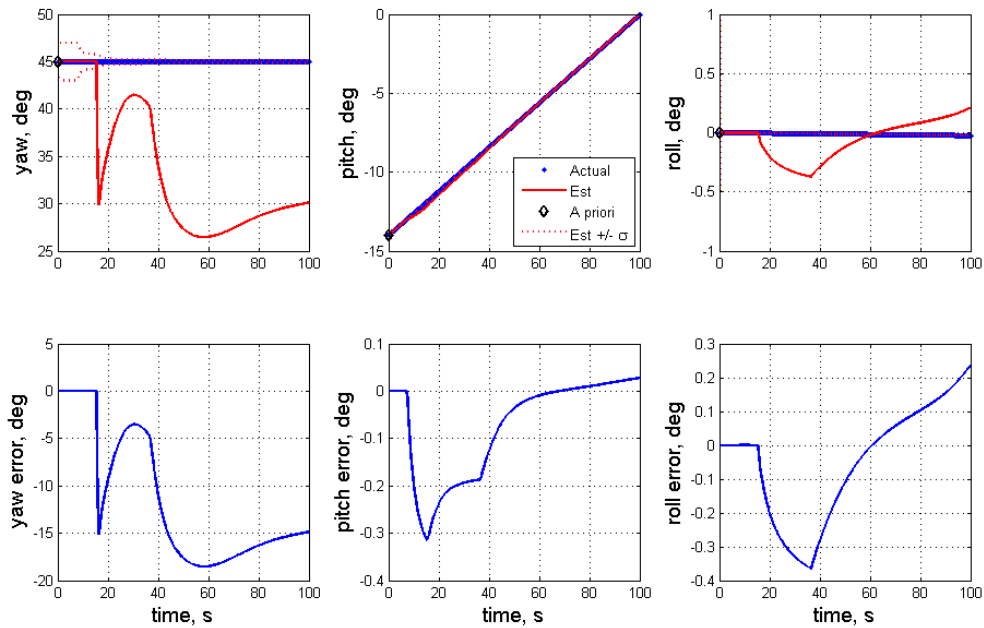


Figure 31. Influence of step terrain on orientation estimates.

The impact of the individual beams on the step can be seen in Figure 27, with beam 1 impacting at 7 seconds, beam 2 at 15 seconds, and beam 3 at 37 seconds. Note that the impact of beam 1 does not contribute a large error in the x and y position estimates; the effect of beams 2 and 3 impacting the step is much greater. Also of note is the altitude estimate, which settles to an estimate of 1 m. This is because the estimate of altitude is in the inertial frame; the filter is actually settling on the top of the step at a height of 1 m. The velocity estimates in Figure 28 show similar results. The impact of beam 1 on the surface does not produce a large error in velocity, but the impacts of beams 2 and 3 do. These velocity errors are again the main contributor to the position errors seen in Figure 27. The estimate in the z direction settles most quickly, with errors in x and y trending toward zero more slowly.

In Figures 29 and 30, the IMU bias estimates again make the beam impact events evident. The impact of beam 1 produces a change in the pitch gyro estimate, with little effect on the other two. However, it also feeds into the estimates of the accelerometer biases. When beam 2 tracks over the step, it produces a change in the roll gyro estimate, and also feeds into all directions of the accelerometer bias estimates. Finally, when beam 3 impacts, it produces a change in the yaw gyro bias estimate. While there is of course some effect of each impact on estimates in all three directions, each produces a much larger effect in one direction than in the other two. Examining the orientation estimates in Figure 31 can lead to more understanding of the effects. The impact of beam 1 produces primarily a change in the pitch estimate, as expected. When beam 2 impacts, it produces a change in the roll estimate. At the same time, the yaw estimate is affected. Because yaw cannot be determined for a flat surface, the change is much larger than the roll change.

However, because the surface is not entirely flat (due to the step), there is some activity in estimating the yaw. When beam 3 impacts the step, both the pitch and roll estimates are affected, and they begin to trend towards the true state. However, because of the large errors in the gyro bias estimates, the estimated angles do not return precisely to the true state.

These results show that while this type of terrain can introduce errors into the spacecraft state estimate, landing would still be possible. While errors in the landing location would be off by over 100m in each direction, the spacecraft would still come to rest on the surface. Velocities in all directions upon landing would still be minimal. The orientation of the spacecraft would also be tolerable. While the yaw estimate is off by 15 degrees from the true state, pitch and roll estimates are correct to within a fraction of a degree. Because yaw cannot be determined, such large errors might be expected. However, with the more accurate pitch and roll estimates, as well as the minimal velocities nearing the surface, landing would still be possible. Further retuning of the filter to better estimate the gyro biases and reduce influence on the yaw estimate is a subject of interest for possible further research.

## 6 Conclusions and Future Work

A retuned Kalman filter for accurately estimating spacecraft position, velocity, and orientation during landing has been presented. This filter combines IMU measurements of acceleration and angular velocity with LIDAR measurements of range and line of sight Doppler velocity for increased accuracy in state estimation. This filter, originally tuned for use over a flat surface, now provides a more accurate estimate over

realistic rough terrains. This retuned filter will allow for greater landing accuracy for future unmanned or human missions to the Moon or Mars, allowing them to land near sites of scientific interest, or in possibly hazardous areas.

This filter has been found to be robust, even when misalignments are present in the LIDAR geometry, or if limited data is available. The filter is capable of accurately estimating the state for various polar angles, but the current beam geometry provides a good balance in the accuracy of the estimates. The retuned filter has been tested through extensive simulation and shown to provide accurate state estimates over terrains including hemispherical bumps, sinusoidal ridges, and steps.

Recommendations for further work include: attempting to relate the range and Doppler measurements more accurately; running more simulations over additional types of terrains; and developing an algorithm for automatic tuning of the filter based on an elevation map of the expected terrain. Perhaps most importantly, the filter should be implemented into the hardware for the next series of test flights, so that the filter estimate of the spacecraft state can be tested in real-time.

# References

Aitken, M.L., *LIDAR-Aided Inertial Navigation with Extended Kalman Filtering for Pinpoint Landing*. MS thesis. North Carolina State University, Raleigh, NC. 2009.

Amzajerjian, F. (PI), Pierrottet, D., Tolson, R., Powell, R., Davidson, J., and Peri, F. "Development of a Coherent Lidar for Aiding Precision Soft Landing on Planetary Bodies," NASA Technical Report, 2005.

Bennett, F.V., and Price, T.G., "Study of Powered-Descent Trajectories for Manned Lunar Landings," NASA Technical Note D-2426, 1964.

Johnson, A., Klumpp, A., Collier, J., and Wolf, A., "Lidar-based Hazard Avoidance for Safe Landing on Mars," American Institute of Aeronautics and Astronautics, Inc., Reston, VA, 2001.

Lefferts, E.J., Markley, F.L., and Shuster, M.D., "Kalman Filtering for Spacecraft Attitude Estimation," *Journal of Guidance, Control, and Dynamics*, Vol. 5, 1982, pp 417-429.

Pierrottet, D., Amzajerjian, F., Petway, L., Barnes, B., and Lockard, G., "Flight Test Performance of a High Precision Navigation Doppler Lidar," NASA Technical report LF99-8520, 2009.

Trawny, N., Mourikis, A.I., Roumeliotis, S.I., Johnson, A.E., and Montgomery, J.F., "Vision-Aided Inertial Navigation for Pin-Point Landing using Observations of Mapped Landmarks," *Journal of Field Robotics*, Vol. 24, No. 5, 2007, pp 357-378.

Vallado, D.A., *Fundamentals of Astrodynamics and Applications*, Microcosm Press, Hawthorne, CA, 2007.